Enhanced Alkaline Hydrogen Evolution on $Gd_{1.0}/Nd_x$ (x = 0.5, 1.0, 3.0, and 6.0%)-Doped TiO_2 Bimetallic Electrocatalysts

Mohammed Alsawat [1,*], Naif Ahmed Alshehri [2], Abdallah A. Shaltout [3], Sameh I. Ahmed [4], Hanan M. O. Al-Malki [1], Manash R. Das [5,6], Rabah Boukherroub [7], Mohammed A. Amin [1,*] and Mohamed M. Ibrahim [1,*]

[1] Department of Chemistry, College of Science, Taif University, Taif 21944, Saudi Arabia; hh.1818@hotmail.com
[2] Physics Department, College of Science, Al-Baha University, Aqiq, Al-Baha 65431, Saudi Arabia; nalshehri@bu.edu.sa
[3] Spectroscopy Department, Physics Research Institute, National Research Centre, El Behooth St., Dokki, Cairo 12622, Egypt; aa.shaltout@nrc.sci.eg
[4] Department of Physics, College of Science, Taif University, Taif 21944, Saudi Arabia; sameh2977@gmail.com
[5] Advanced Materials Group, Materials Sciences and Technology Division, CSIR-North East Institute of Science and Technology, Jorhat 785006, India; mrdas@neist.res.in
[6] Academy of Scientific and Innovative Research (AcSIR), Ghaziabad 201002, India
[7] Centre National de la Recherche Scientifique, Université Lille, Université Polytechnique Hauts-de-France, UMR 8520, IEMN, F-59000 Lille, France; rabah.boukherroub@univ-lille.fr
[*] Correspondence: mosawat@tu.edu.sa (M.A.); mohamed@tu.edu.sa (M.A.A.); ibrahim@tu.edu.sa (M.M.I.)

Abstract: The work reports a facile synthesis of high thermally stable nanocrystalline anatase TiO_2 nanoparticles (NPs) doped with different atomic concentrations (0.5, 1.0, 3.0, and 6.0%) of Gd^{3+} and Nd^{3+} ions by a template-free and one-step solvothermal process, using titanium(IV) butoxide as a titanium precursor and dimethyl sulfoxide (DMSO) as a solvent. The structure and morphology of the Gd^{3+}, Nd^{3+}, and 0.5%Gd^{3+}-0.5%Nd^{3+}/doped TiO_2 NPs have been characterized by using various analytical techniques. The Gd^{3+}/ and Nd^{3+}/TiO_2 molar ratios were found to have a pronounced impact on the crystalline structure, size, and morphology of TiO_2 NPs. X-ray diffraction (XRD) and X-ray photoelectron spectroscopy (XPS) studies revealed the proper substitution of Ti^{4+} by Gd^{3+} and Nd^{3+} ions in the TiO_2 host lattice. The as-prepared Gd_x/TiO_2, Nd_x/TiO_2, and $Gd_{1.0}/Nd_x/TiO_2$ bimetallic NPs, x = 0.5, 1.0, 3.0, and 6%, have been investigated as electrocatalysts for hydrogen evolution reaction (HER) in 1.0 M KOH solution using a variety of electrochemical techniques. At any doping percentage, the $Gd_{1.0}/Nd_x/TiO_2$ bimetallic NPs showed higher HER catalytic performance than their corresponding counterparts, i.e., Gd_x/TiO_2 and Nd_x/TiO_2. Upon increasing the Nd content from 0.5 to 6.0%, the HER catalytic performance of the $Gd_{1.0}/Nd_x/TiO_2$ bimetallic NPs was generally enhanced. Among the studied materials, the bimetallic $Gd_{1.0}/Nd_{6.0}/TiO_2$ NPs emerged as the most promising catalyst with an onset potential of −22 mV vs. RHE, a Tafel slope of 109 mV dec^{-1}, and an exchange current density of 0.72 mA cm^{-2}. Such HER electrochemical kinetic parameters are close to those recorded by the commercial Pt/C (onset potential: −15 mV, Tafel slope: 106 mV dec^{-1}, and exchange current density: 0.80 mA cm^{-2}), and also comparable with those measured by the most active electrocatalysts reported in the literature. The synergistic interaction of Gd and Nd is thought to be the major cause of the bimetallic catalyst's activity.

Keywords: titanium dioxide; rare earth-doped TiO_2 nanoparticles; electrochemical; hydrogen generation; alkaline

1. Introduction

The ever-growing demand for clean, renewable, environmentally friendly, and cost-effective energy sources has resulted from meeting the needs of modern society, which is expanding and evolving quickly. Utilizing hydrogen (H_2) as a possible energy source with the possibility of replacing fossil fuels has proven to be a particularly alluring strategy in this context,

partly because of its high combustion heat (287 kJ/mol) and the release of green byproduct water [1]. A significant portion of H_2 is produced from fossil fuels using a steam reforming method that also produces CO_2, which is thought to be a potential cause of environmental global warming [2].

One of the most advantageous processes for producing very pure H_2 gas is alkaline water electrolysis. The effectiveness of alkaline water electrolysis is, however, constrained by the sluggish kinetics of the hydrogen evolution process (HER) in alkaline media [3–5]. Effective electrocatalysts are suggested for use as cathode materials in water electrolysis cells because they produce significant amounts of H_2 at low overpotentials by accelerating the kinetics of the HER. Electrode materials based on platinum (Pt) are the most reliable and effective HER electrocatalysts. The excessive cost of these components, however, raises the price of water electrolyzers. As a result, one of the primary goals for the efficient production of H_2 on a large scale is the deployment of innovative, affordable, and effective HER electrocatalysts [6,7].

For the purpose of achieving good electrochemical performances, researchers have designed nanostructures of various Pt group metals (Ru, Rh, Ir, and Pd) with high surface-to-volume ratios [8]. Nitrogen-doped reduced graphene oxide (rGO)-based Pt-TiO_2 nanostructures [9], monolayer Pd and Au supported on Mo_2C [10], monolayer Pt supported on bulk tungsten carbide (WC) [11], etc., were employed as HER electrocatalysts, demonstrating outstanding activity.

Extensive research has been conducted on alternative non-noble (Fe, Co, Ni, Mo), MoS_2 coupled with a perovskite oxide, and metal-free (carbon-based) electrocatalysts in an effort to avoid using precious noble metals [12–17]. Transition metal chalcogenides [18], carbides [19], metal alloys [20], and complexes [21] are examples of other non-noble electrocatalysts. Bimetallic NPs, which are composed of two elements, have drawn a lot of attention for their efficiency as HER electrocatalysts as well as for their potential use in a variety of energy storage applications [22–25]. They have greater catalytic characteristics compared to their monometallic counterparts, which is primarily ascribed to their improved and tunable chemical, physical, and cooperative interactions [25,26]. Au-Pd [27,28] and Au-Ni [29] bimetallic electrocatalysts exhibited high catalytic performance for the HER among bimetallic alloys. Excellent HER activity may be found in alloy nanostructures made of Cu-Pt [30], Au-Pt [31], and other metals. Core-shell nanostructures can also take the place of Pt in a number of HER reactions. Examples of outstanding performances include Au@Pt [32], Cu@Pd/Ti [33], Au@Pd [34], Au@Pd [35], and Au@CdS core-shell nanostructures [36].

In this work, a facile synthesis of Gd^{3+} and Nd^{3+}-doped TiO_2 NPs at different atomic concentrations (0.5, 1.0, 3.0, and 6.0%) of Gd^{3+} and Nd^{3+} ions, as well as the mixed 0.5%Gd^{3+}-0.5%Nd^{3+}-doped TiO_2 NPs, using titanium(IV) butoxide as a titanium precursor and dimethyl sulfoxide (DMSO) as a solvent, is presented. The lack of usage of amphiphilic surfactants, capping agents, or block copolymers, in contrast to the majority of earlier preparation techniques, can significantly reduce production cost of the synthesized catalysts. Our process is highly straightforward, economical, and easily scalable, as it required only three basic ingredients. The reducing agent and stabilizing layer in this approach were both performed by the DMSO solvent, which is believed to adhere to the surface of the NPs, preventing their agglomeration.

The structure and morphology of the obtained doped TiO_2 NPs, namely, Gd_x/TiO_2, Nd_x/TiO_2, and $Gd_{1.0}/Nd_x/TiO_2$ bimetallic NPs, x = 0.5, 1.0, 3.0, and 6%, were characterized by advanced surfaces analysis techniques. Using linear sweep voltammetry, the newly synthesized electrode materials were assessed for the first time as HER electrocatalysts in 1.0 M KOH aqueous solution. Chronoamperometry and repetitive cyclic polarization measurements were used to evaluate the stability of the best performing electrocatalyst.

2. Results and Discussion

2.1. Characterization of Gd_x/TiO_2, Nd_x/TiO_2, and $Gd_{0.5}/Nd_{0.5}/TiO_2$ NPs

The formation of Gd_x/TiO_2, Nd_x/TiO_2, and $Gd_{0.5}/Nd_{0.5}/TiO_2$ NPs was characterized by Fourier-Transform Infrared Spectroscopy (FT-IR) and simultaneous Thermogravimetric Analysis-Differential Thermal Analysis (TGA-DTA) (Supporting information, Figures S1 and S2).

Energy dispersive X-ray fluorescence (EDXRF) was used to quantify the elemental contents of the Gd_x/TiO_2, Nd_x/TiO_2, and $Gd_{0.5}/Nd_{0.5}/TiO_2$ NPs. Before carrying out the EDXRF measurements, a series of Gd_x/TiO_2, Nd_x/TiO_2, and $Gd_{0.5}/Nd_{0.5}/TiO_2$ NPs were homogenously distributed inside the powder sample holder of 25 mm diameter. Mylar foil (4.5 μm-thick, Chemplex Industries, Inc., Palm City, FL, USA) was installed inside the sample holder. Furthermore, fine powders of Gd_x/TiO_2, Nd_x/TiO_2 and $Gd_{0.5}/Nd_{0.5}/TiO_2$ NPs were also prepared and measured under the same conditions. Based on the direct excitation from the X-ray tube, only the characteristic radiation of Nd, Gd, and Ti was detected, Figures 1–3. As illustrated in Figures 1–3, the characteristic Kα and Kβ lines of Ti were free from spectral interference and were detected at photon energies of 4.509 and 4.932 keV, respectively. Additional sum peaks of Ti were recognized at photon energies of 9.019 and 9.452 keV. Using the EDXRF spectra of the current nanocomposites, standard-less quantitative elemental analysis based on the fundamental parameter approach was performed. The proposed method is based on the conversion of the measured intensities (primary, secondary, and ternary) of each element of interest to concentrations in wt.%. Standard-less software "UniQuant" delivered from the manufacturer was utilized for this purpose. The current method has many advantages, such as how fast it is, its simplicity, complete absence of the standard materials, and automatic matrix correction. Figures 1 and 2 depict the X-ray fluorescence spectra of the Gd_x/TiO_2 and Nd_x/TiO_2 series at different concentrations of Gd and Nd ranging from 0.5 to 6 wt.%. The characteristic L lines of Gd were detected, and all of them are free from spectral interferences. The detected Gd-L lines are $L\alpha_1$, $L\beta_1$, $L\beta_2$, $L\gamma_1$, $L\gamma_2$, and L_ι at photon energies of 6.058, 6.714, 7.103, 7.786, 8.084, and 5.36 keV, respectively, Figures 1 and 3. The characteristic radiations of $Nd-L\alpha_1$, $Nd-L\beta_1$, $Nd-L\beta_2$ were recognized at 5.231, 5.722, and 6.09 keV, respectively, Figures 2 and 3. In the case of the $Gd_{0.5}/Nd_{0.5}/TiO_2$ NPs, there was a spectral interference between $Nd-L\beta_2$ at 6.09 keV and $Gd-L\alpha_1$, which was located at 6.058 keV, Figure 3. Additional spectral interferences between $Nd-L\gamma_1$ and $Gd-L\beta_1$ were observed at 6.602 and 6.714 keV, respectively. Although there was a remarkable spectral interference between L lines of Nd and Gd, the $Nd-L\alpha_1$ and $Nd-L\beta_1$ at, respectively, 5.231 and 5.722 keV were free from interference and can be used. In addition, the $Gd-L\beta_2$ at 7.103 keV and $Gd-L\gamma_1$ at 7.786 keV were also free from spectral interference. As shown in Figures 1 and 2, the characteristic L lines of Gd and Nd increase as the concentration of Gd and Nd increases. The quantitative elemental analysis results of the Gd_x/TiO_2 and Nd_x/TiO_2 NPs are presented in Table 1. The obtained concentrations (wt.%) of both Gd_x/TiO_2 and Nd_x/TiO_2 NPs are almost in good agreement with the initial prepared ratios. Table 2 summarizes the quantitative elemental analysis results of $Gd_{0.5}/TiO_2$, $Nd_{0.5}/TiO_2$, and $Gd_{0.5}/Nd_{0.5}/TiO_2$ NPs. In the case of $Gd_{0.5}/Nd_{0.5}/TiO_2$ NPs, the L lines of Gd and Nd are close to Ti-K lines and below 10 keV. The obtained results are in accordance with expected ratios.

X-ray diffraction (XRD) was employed to check the Gd^{3+}- and Nd^{3+}-doped TiO_2 phases and their crystallinity. Both Gd_x/TiO_2 and Nd_x/TiO_2 (x = 0.5, 1.0, 3.0, and 6.0 wt.%) samples only comprised diffraction peaks of the tetragonal anatase phase (JCPDS # 01-084-1286) [37]. No peaks for any oxide byproducts were observed for all the samples, most probably due to the XRD detection limit. This reflects the substitution of both Gd and Nd (up to 6%) in the TiO_2 anatase lattice forming a homogeneous solid solution. The structural information for all the refined phases was obtained by Rietveld refinements [38,39]. The anatase phase with the tetragonal lattice was refined in the space group $I4_1/amd$ [40] and dominated the composition of all TiO_2 samples (Table 1). Figure 4a–c shows the calculated

and observed diffraction patterns from Rietveld refinement for three selected samples where R_{wp} (%) = 4 to 5.
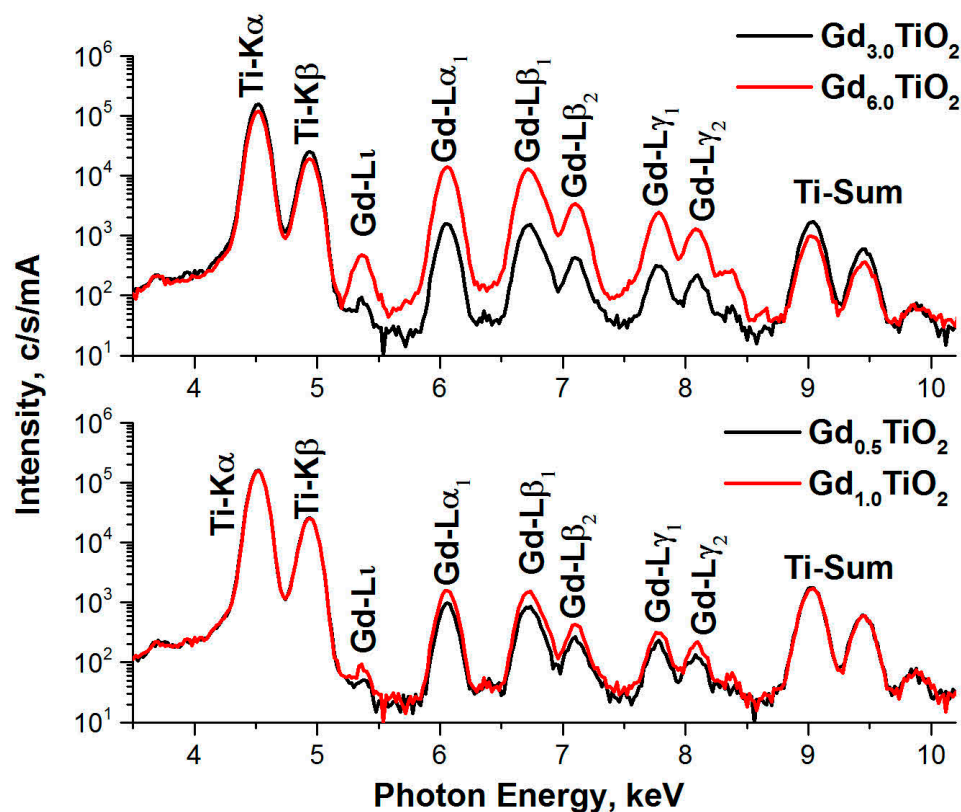

Figure 1. The EDXRF spectra of the Gd_x/TiO_2 nanocomposites.
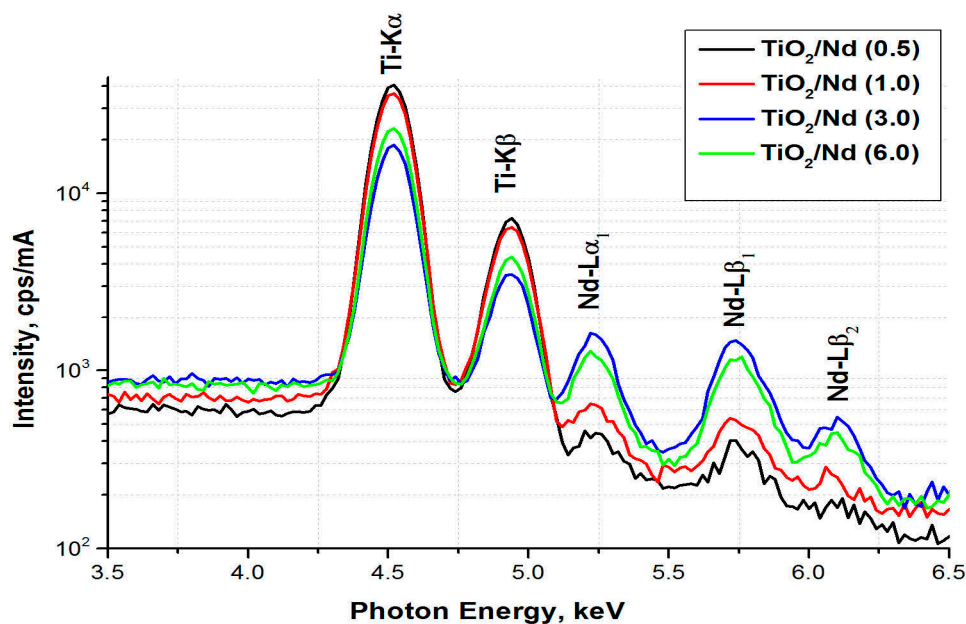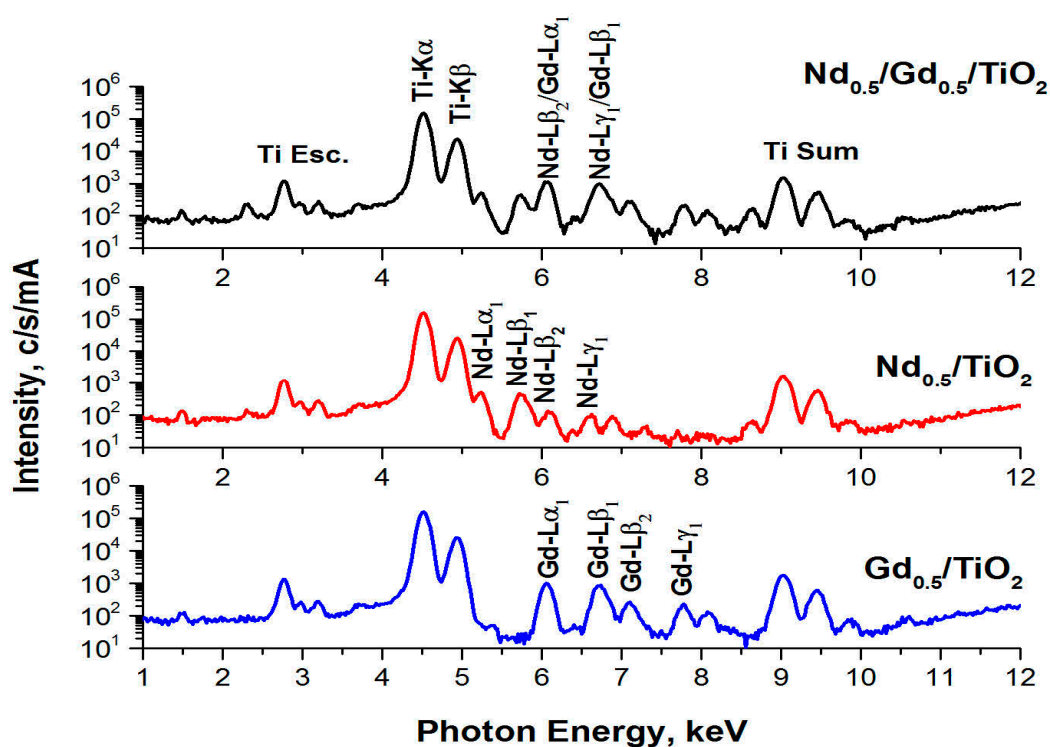

Figure 2. The EDXRF spectra of the Nd_x/TiO_2 nanocomposites.

Figure 3. The EDXRF spectra of the $Gd_{0.5}/TiO_2$, $Nd_{0.5}/TiO_2$, and $Gd_{0.5}/Nd_{0.5}/TiO_2$ nanocomposites.

Table 1. Elemental quantitative analysis in wt.% of the Gd_{xx}/TiO_2 and Nd_{xx}/TiO_2 composites using Energy dispersive X-ray fluorescence (EDXRF) analysis.

Gd$_x$/TiO$_2$ Composites			Nd$_x$/TiO$_2$ Composites		
Sample	Gd, %	TiO$_2$, %	Sample	Nd, %	TiO$_2$, %
$Gd_{0.50}/TiO_2$	1.80 ± 0.06	97.92 ± 0.07	$Nd_{0.5}/TiO_2$	1.13 ± 0.05	98.67 ± 0.06
$Gd_{1.0}/TiO_2$	2.20 ± 0.07	97.46 ± 0.08	$Nd_{1.0}/TiO_2$	2.16 ± 0.07	97.45 ± 0.08
$Gd_{3.0}/TiO_2$	2.39 ± 0.07	97.24 ± 0.08	$Nd_{3.0}/TiO_2$	7.71 ± 0.12	90.95 ± 0.14
$Gd_{6.0}/TiO_2$	3.07 ± 0.08	96.45 ± 0.09	$Nd_{6.0}/TiO_2$	10.89 ± 0.25	87.19 ± 0.17

Table 2. Elemental quantitative analysis in wt.% of the $Gd_{0.5}/TiO_2$, $Nd_{0.5}/TiO_2$ and $Gd_{0.5}/Nd_{0.5}/TiO_2$ composites using EDXRF.

Sample	Gd$_{0.5}$/TiO$_2$	Nd$_{0.5}$/TiO$_2$	Gd$_{0.5}$/Nd$_{0.5}$/TiO$_2$
Gd	2.01 ± 0.07	-	2.11 ± 0.07
Nd	-	1.13 ± 0.05	1.04 ± 0.05
TiO$_2$	97.85 ± 0.07	98.67 ± 0.06	96.35 ± 0.09

Figure 4d–f displays the tetragonal lattice parameters and the cell volume of the anatase phase as a function of Gd content. According to Vegard's law [41], the cell parameter *a* increased, which was attributed to the replacement of Ti with larger Gd atoms inside the anatase lattice. On the other hand, the cell parameter *c* decreased upon increasing the doping content and could be understood as a relaxation of the lattice due to the expansion of the *a* cell parameter. In turn, the volume of the anatase tetragonal cell was dominated by the enlargement of the *a* parameter and featured a slight increase with increasing the Gd and Nd content. In addition, the crystallite size was about 20 nm in the case of Gd doping, while doping with Nd reduced the crystallite size to about 10 nm, Table 3.
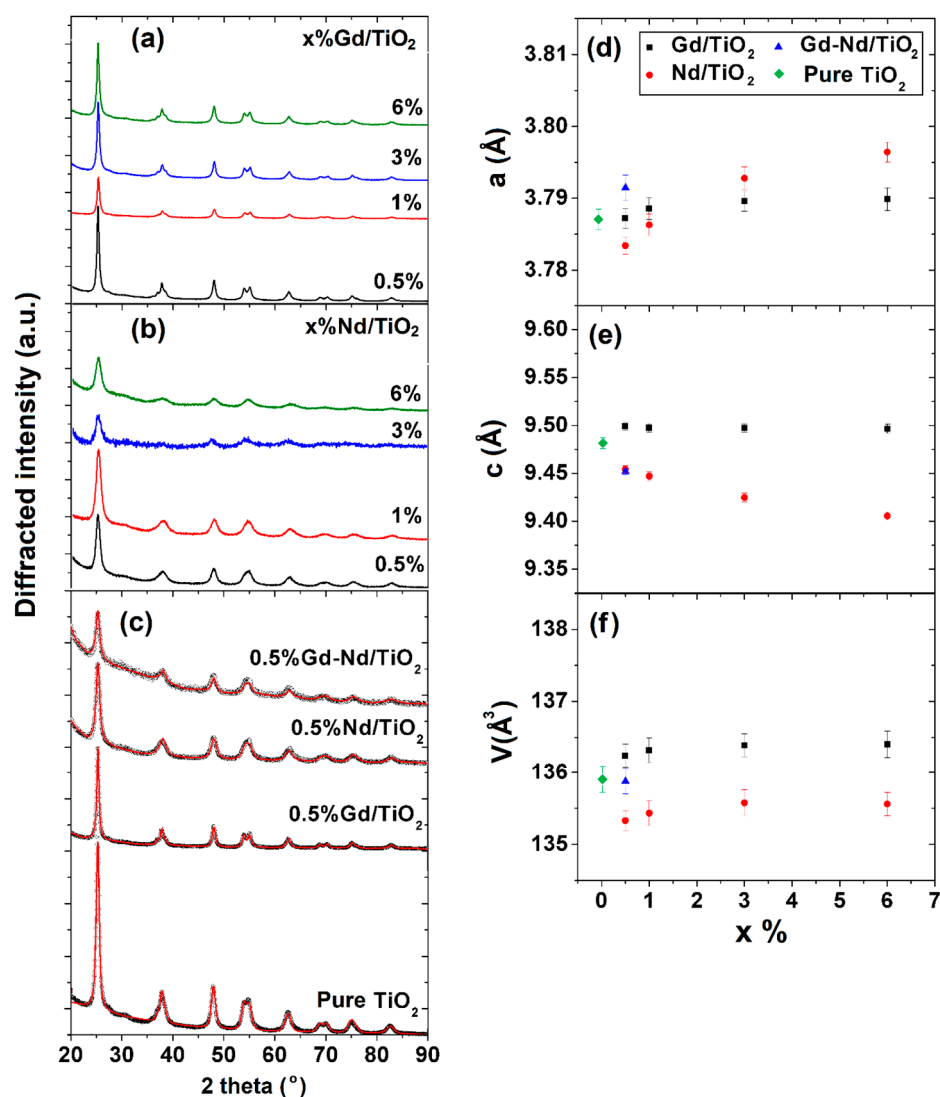
Figure 4. XRD patterns of (**a**) Gd_x/TiO_2 NPs and (**b**) Nd_x/TiO_2 NPs, (**c**) calculated (red) and recorded (black) diffraction patterns of $Gd_{0.5}/TiO_2$, $Nd_{0.5}/TiO_2$ and $Gd_{0.5}/Nd_{0.5}/TiO_2$, (**d,e**) lattice parameters as a function of Gd and Nd content, (**f**) cell volume as a function of Gd and Nd content.

Table 3. The cell parameters and crystallite size of Gd_x/TiO_2, Nd_x/TiO_2, and $Gd_{0.5}/Nd_{0.5}/TiO_2$ NPs as calculated from the Rietveld refinements.

| x	Gd_x/TiO_2				Nd_x/TiO_2			
	a (A)	c (A)	V (A³)	D (nm)	a (A)	c (A)	V (A³)	D (nm)
0.5	3.7872 (14)	9.499 (4)	136.24 (16)	21 (2)	3.7834 (12)	9.454 (4)	135.33 (14)	12 (1)
1.0	3.7885 (15)	9.497 (5)	136.31 (17)	19 (2)	3.7863 (15)	9.447 (5)	135.43 (17)	11 (1)
3.0	3.7895 (14)	9.497 (4)	136.39 (16)	18 (1)	3.7928 (16)	9.425 (5)	135.58 (18)	10 (2)
6.0	3.7899 (16)	9.496 (5)	136.40 (18)	18 (1)	3.7964 (14)	9.405 (4)	135.56 (16)	10 (2)
	0.5%Gd-0.5%Nd/TiO₂				Pure TiO₂			
	3.7915 (18)	9.452 (3)	135.87 (17)	12 (2)	3.7854 (14)	9.4842 (5)	135.9 (17)	17 (3)

2.2. Composition and Chemical State Analysis

The composition and chemical state of pure TiO_2, Gd_x/TiO_2, Nd_x/TiO_2, and $Gd_{0.5}/Nd_{0.5}/TiO_2$ NPs were characterized by electron spectroscopy for chemical analysis (ESCA) set up using a monoenergetic Al-Kα (1486.6 eV). Figure 5 exhibits the survey spectrum of the

pure TiO_2 nanoparticles as well as the core level spectra of the Ti 2p and O 1s. The core levels plot of Ti and O were recognized not only in the pure TiO_2, but also in the doped TiO_2, Figures 5–7. The peak of the C 1s at 284.6 eV as well as the KVV Auger line at 1233 eV originate from the adsorption of carbon on the surface due to contamination. The C 1s peak was used as a reference to correct the charge shift in the doped TiO_2 [42]. Two principle peaks of Ti 2p at the binding energies of 458.8 and 464.4 eV were allocated to Ti $2p_{3/2}$ and Ti $2p_{1/2}$, respectively. Besides, the Ti Auger lines were assigned to $LM_{23}M_{23}$ and $L_3M_{23}M_{45}$ at 1103 and 1073 eV, respectively. The spin-orbit splitting of 5.7 eV between the two peaks of Ti 2p confirms the existence of titanium dioxide [43]. Therefore, the oxidation state of titanium is mostly +4, and this is consistent with the literature data.
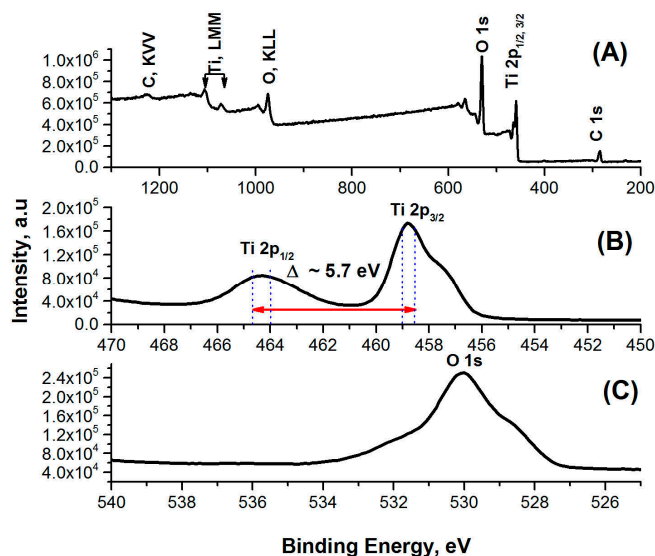
Figure 5. X-ray photoelectron spectroscopy analysis of the pure TiO_2 nanoparticles including (**A**) a survey and core level spectra of (**B**) Ti 2p and (**C**) O 1s.
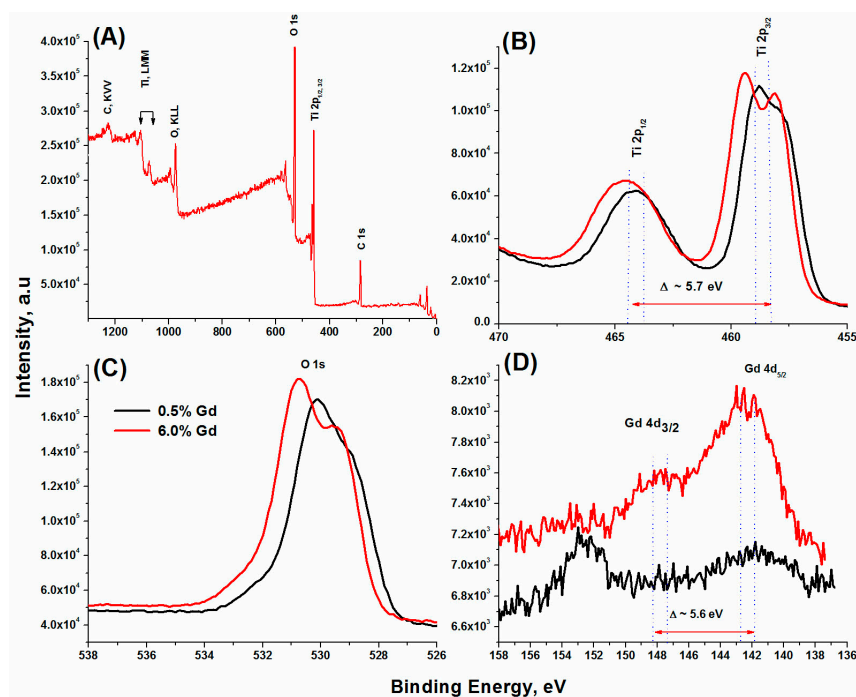
Figure 6. X-ray photoelectron spectroscopy of the Gd/TiO_2 nanoparticles at 0.5% and 6.0% of Gd including (**A**) a survey and core level spectra of (**B**) Ti 2p, (**C**) O 1s, and (**D**) Gd 4d.
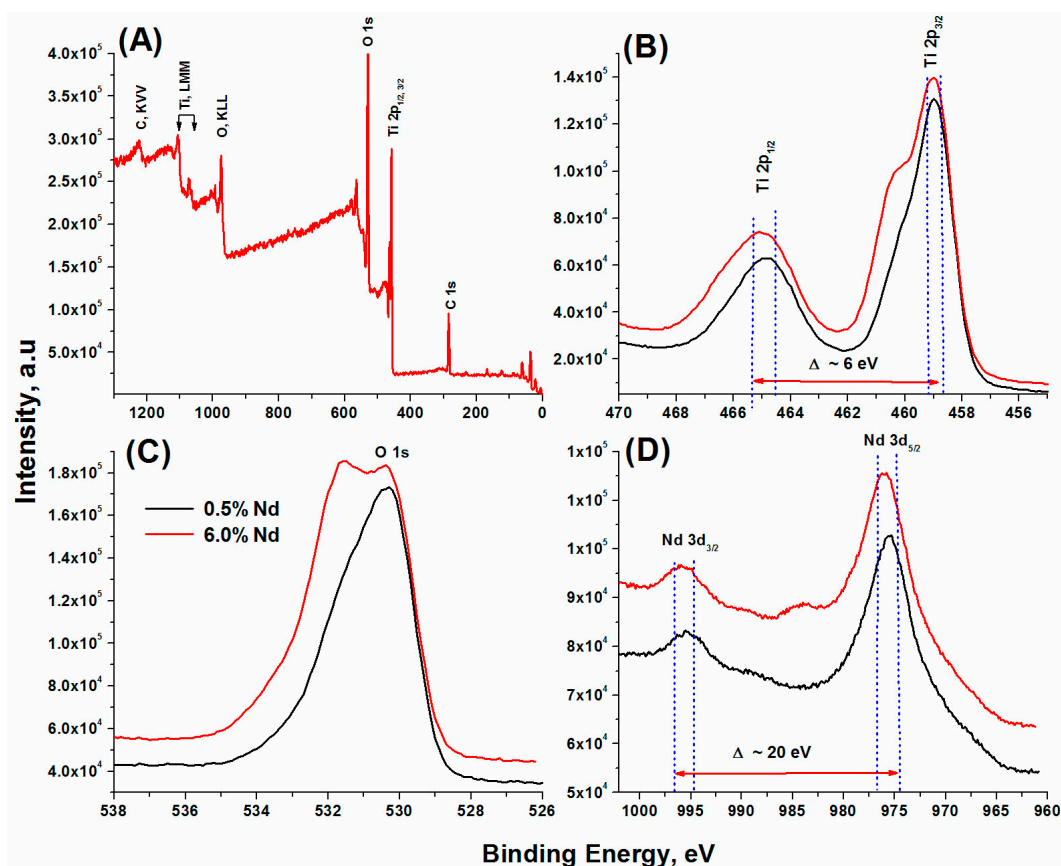
Figure 7. X-ray photoelectron spectroscopy of the Nd-doped TiO$_2$ nanoparticles at 0.5 and 6.0 wt.% of Nd including (**A**) a survey and core spectra of (**B**) Ti 2p, (**C**) O 1s, and (**D**) Nd 3d.

The shifts of the Ti 2p to high binding energy with Gd and Nd could be attributed to either new species of the TiO$_2$ or the inelastic scattering of Gd and Nd atoms within the anatase crystal structure [44].

The peak of O 1s was estimated at 530.1 eV at the low content of doping (0.5%). At the high doping level (6.0%) of Gd and Nd, two peaks of O 1s were observed at 529.8 and 530.7 eV, respectively, Figures 6 and 7. The different oxygen species could be the main reason for the shoulder at higher binding energy. Additional KLL Auger lines could be recognized at around 1000 eV. The two peaks of O 1s in the doped TiO$_2$ were attributed to the crystal lattice oxygen at 529.8 eV and hydroxyl oxygen (Ti-OH) for pure TiO$_2$ at 530.7 eV, Figures 6 and 7 [45]. However, the different oxygen species could be the main reason for the shoulder at higher binding energy. As the concentrations of Gd and Nd increase from 0.5% to 6% in the anatase phase, remarkable shifts of the O 1s peak was observed, which suggests the presence of Gd$_2$O$_3$ and Nd$_2$O$_3$ in the anatase crystal [46,47]. Additionally, the remarkable shifts of the O 1s peak could be attributed to the surface relaxation effects [48].

In the case of Gd-doped TiO$_2$, two weak peaks of Gd were identified at 142 and 152 eV ascribed to 4p3/2, 4d5/2, respectively, Figure 6. Due to the low detector efficiency at high Z elements, the statistical distribution of the Gd 4d peaks was poor, and the Gd 3d peaks could not be detected at a low concentration of Gd (0.5%). The binding energy of Gd 4d$_{5/2}$ at 142.4 eV indicates the trivalent oxidation state of gadolinium, mostly in the form of Gd$_2$O$_3$, which is in agreement with reference [49].

The spin orbit splitting between the two peaks of Gd 4d equals 5.6 eV, and it also agrees with the literature [49]. Based on the obtained spectra of Gd$_x$/TiO$_2$ NPs, the characteristic peaks of Gd were successfully evidenced in the TiO$_2$, Figure 6. The valence state of Nd$_x$/TiO$_2$ NPs was also demonstrated. The complete doping behavior was also confirmed

in the case of Nd $_x$/TiO$_2$ NPs. The two characteristic peaks of Nd 3d$_{3/2}$ and Nd 3d$_{5/2}$ were located, respectively, at 995.8 and 975.9 eV, Figure 7. The values of the binding energy of Nd 3d agree with those reported by Wang et al. [50]. The spin orbit splitting between the two peaks of Nd 3d equals 20 eV, Figure 7.

As seen from Figures 5–8, the intensity of O 1s peak decreased after doping with Gd or Nd compared with the pure TiO$_2$, which confirms the successful doping in TiO$_2$. In the case of Gd$_x$/TiO$_2$ and Nd$_x$/TiO$_2$ NPs, the binding energies (BE) of the two peaks of Ti 2p$_{1/2}$ and 2p$_{3/2}$ at 464.8 and 458.9 eV, respectively, are lower than those of pure TiO$_2$. Besides, the BE of the two peaks of Ti in Gd$_x$/TiO$_2$ are also lower than those of Nd$_x$/TiO$_2$ NPs, Figures 5–8. The decrease in Ti 2p BE might be attributed to the Ti^{4+} and O^{2-} local environment change by the introduction of Gd or Nd atoms.
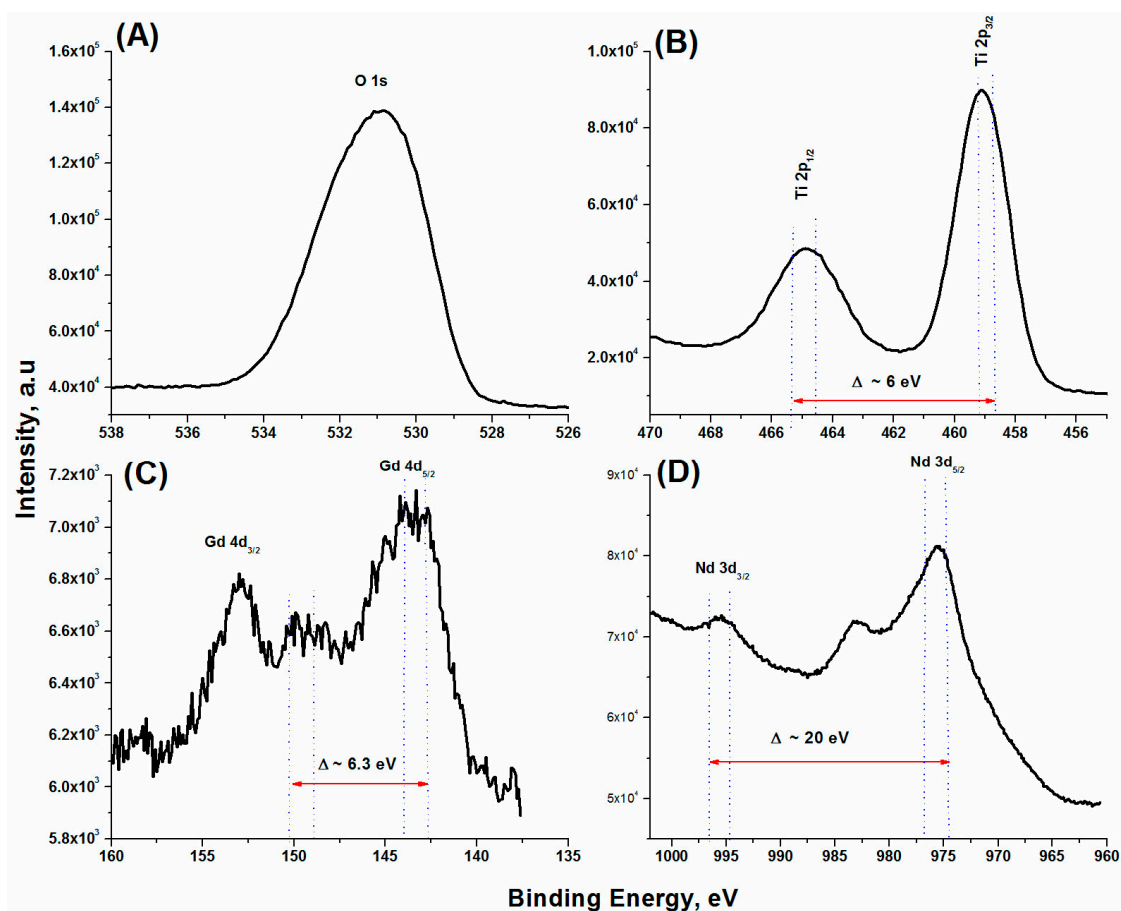
Figure 8. XPS core level spectra of (**A**) O 1s, (**B**) Ti 2p, (**C**) Gd 4d, and (**D**) Nd 3d of the Gd$_{0.5}$/Nd$_{0.5}$/TiO$_2$ NPs.

As shown in Figures 6 and 7, these shifts in the BE of Ti 2p and O 1s peaks could be ascribed to the formation of Ti –Gd and Ti–Nd bonds on the grain boundaries of the crystallites, reducing the Ti^{4+} BE. Figures 6 and 7 revealed an increase of Nd 3d and Gd 4d peak intensities upon increasing the doping level from 0.5 to 6.0 wt.%. At a concentration of 0.5 wt.% of Nd and Gd, the O 1s and Ti 2p intensities had a remarkable decrease. The spin orbit splitting of Nd 3d and Gd 4d remained the same as the previous cases.

Tables 4–7 summarize the measured binding energies, full widths at half maximum (FWHM), peak areas, and atomic concentrations for pure TiO$_2$, Gd$_x$/TiO$_2$ and Nd$_x$/TiO$_2$ NPs, and Gd$_{0.5}$/Nd$_{0.5}$/TiO$_2$ NPs. The non-stoichiometric atomic ratios of O:Ti of TiO$_2$ could be ascribed to two main reasons. The first one is the quantitative surface analysis capability of the XPS is limited to a few nanometers (1–10 nm). Secondly, due to the chemical treatments of TiO$_2$, Gd$_x$/TiO$_2$ and Nd$_x$/TiO$_2$ NPs, and Gd$_{0.5}$/Nd$_{0.5}$/TiO$_2$ NPs [51], the

atomic ratios of O:Ti of TiO_2 could be relatively non-stoichiometric, especially at the surface of the NPs. As illustrated in Tables 4–6, the O:Ti atomic ratios in Nd_x/TiO_2 samples are higher than those of Gd_x/TiO_2. These results support the reported fact that Nd^{3+} ions are more electropositive than Gd^{3+} ions. Therefore, the Nd doping may create a more oxygen-rich nano-phase structure.

Table 4. The measured binding energies, full widths at half maximum (FWHM), peak areas, and atomic concentrations for the pure TiO_2 NPs.

Peak	Binding Energy (eV)	FWHM (eV)	Peak Area, kcps (eV)	Atomic Conc. (at.%)
O 1s	530.77	7.49	3398.3	73.4
$Ti2p_{1/2}$ $Ti2p_{3/2}$	458.29 463.98	4.74	2892.5	26.5

Table 5. The measured binding energies, full widths at half maxima (FWHM), peak areas, and atomic concentrations for the Gd/TiO_2 NPs.

Peak	Binding Energy (eV)	FWHM (eV)	Peak Area, kcps (eV)	Atomic Conc. (at.%)
		$Gd_{0.5}/TiO_2$		
O 1s	530.77	3.6	991.5	73.43
Ti $2p_{1/2}$ Ti $2p_{3/2}$	458.29 463.98	3.31	973.6	26.48
Gd $4d_{3/2}$ Gd $4d_{5/2}$	142 152	0.27	1.3	0.09
		$Gd_{6.0}/TiO_2$		
O 1s	530.77	3.71	1047.5	71.73
Ti $2p_{1/2}$ Ti $2p_{3/2}$	458.29 463.98	3.23	1049.4	28.11
Gd $4d_{3/2}$ Gd $4d_{5/2}$	142 152	0.0	1.3	0.16

Table 6. The measured binding energies, full widths at half maxima (FWHM), peak areas, and atomic concentrations for the Nd-doped TiO_2 nanoparticles.

| Peak	Binding Energy (eV)	FWHM (eV)	Peak Area, kcps (eV)	Atomic Conc. (at.%)
		Nd (0.5%)/TiO_2		
O 1s	530.77	3.36	1139.1	75.12
Ti $2p_{1/2}$ Ti $2p_{3/2}$	458.29 463.98	1.93	1108.7	24.71
Nd $3d_{3/2}$ Nd $3d_{5/2}$	995.8 975.9	0	0.774	0.17
		Nd (6.0%)/TiO_2		
O 1s	530.77	3.7	1266.5	74.59
Ti $2p_{1/2}$ Ti $2p_{3/2}$	458.29 463.98	3.37	1175.9	25.18
Nd $3d_{3/2}$ Nd $3d_{5/2}$	975.9 995.8	0.01	1.78	0.23

Table 7. The measured binding energies, full widths at half maxima (FWHM), peak areas, and atomic concentrations for the Gd_x/TiO_2 and Nd_x/TiO_2 NPs.

Peak	Binding Energy, eV	FWHM, eV	Peak Area, kcpseV	Atomic Concentration, (at.%)
O 1s	538.5	3.83	961.4	77.55
Ti $2p_{1/2}$ Ti $2p_{3/2}$	458.29 463.98	2.89	657.9	21.82
Gd $4d_{3/2}$ Gd $4d_{5/2}$	142 152	0.19	0.70	0.29
Nd $3d_{3/2}$ Nd $3d_{5/2}$	975.9 995.8	0.64	3.8	0.34

SEM imaging and EDX were used jointly to elucidate the morphology and elemental composition of the Gd_x/TiO_2 and Nd_x/TiO_2 NPs. Figure 9 shows the SEM photographs of the typical Gd_x/TiO_2 and Nd_x/TiO_2 samples. From the images, the Gd_x/TiO_2 and Nd_x/TiO_2 existed essentially in the form of spherical particles and presented porous structures similar to those of TiO_2. The morphological study revealed that for both TiO_2 and Gd_x/TiO_2 samples, the surface looked almost the same with slightly whitish portion, indicating the deposition of Gd. Based on the SEM results, the Ti Kα-fluorescence signals of the pure TiO_2 and Gd_x/TiO_2 samples were also obtained by EDX analysis (Figure 9). Table 8 gives semi-qualitative information about the elemental and atomic percentages in the TiO_2 and Gd_x/TiO_2 samples.
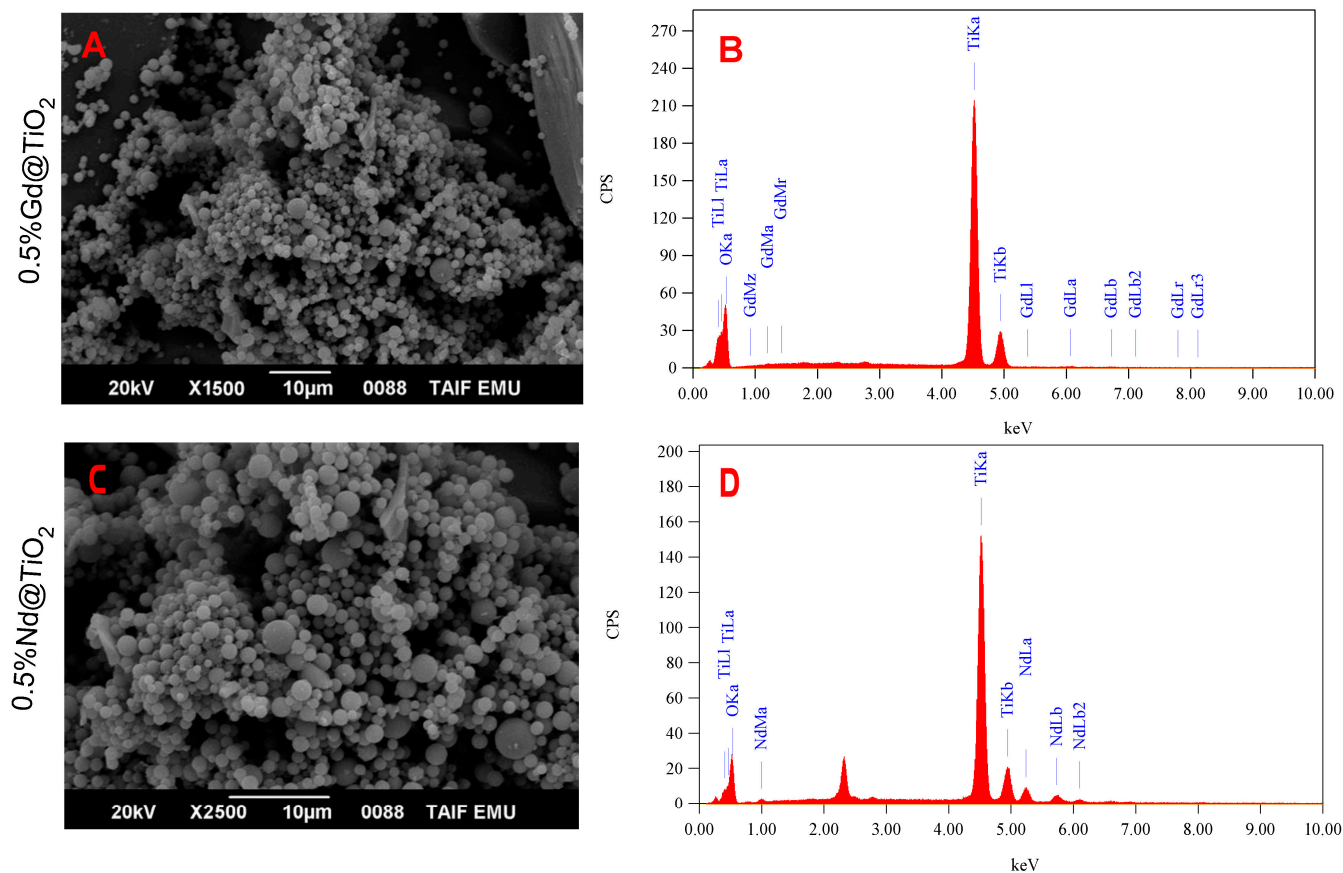

Figure 9. SEM/EDX examinations of $Gd_{0.5}/TiO_2$ (**A**,**B**) and $Nd_{0.5}/TiO_2$ NPs (**C**,**D**).

Table 8. Catalyst composition using EDX analysis of TiO_2, Gd/TiO_2, and Nd/TiO_2.

Element	Compound		
	TiO_2 (Atom%)	Gd_x/TiO_2 (Atom%)	Nd_x/TiO_2 (Atom%)
O	73.04	70.81	72.36
Ti	26.96	29.05	27.46
Gd	-	0.150	-
Nd	-	-	0.185

High Resolution Transmission Electron Microscopy (HR-TEM) Analysis

The morphology of the samples and the corresponding chemical composition were further determined by, respectively, HR-TEM and selected area electron diffraction (SAED) patterns. Figure 10 depicts typical TEM and HR-TEM images (insets SAED patterns) of $Nd_{0.5}/TiO_2$, $Gd_{0.5}/TiO_2$, and $Gd_{0.5}/Nd_{0.5}/TiO_2$ NPs. As evidenced in the TEM images, the majority of the TiO_2 nanoparticles consist mainly of quasi-spherical and cubic particles. The HR-TEM images revealed a characteristic lattice spacing of 0.352 nm for the TiO_2 anatase (101) plane. The average size of both $Gd_{0.5}/TiO_2$ and $Nd_{0.5}/TiO_2$ slightly changed with the increase of the RE^{3+} content; for example, the average particle size range was 10–12 nm.
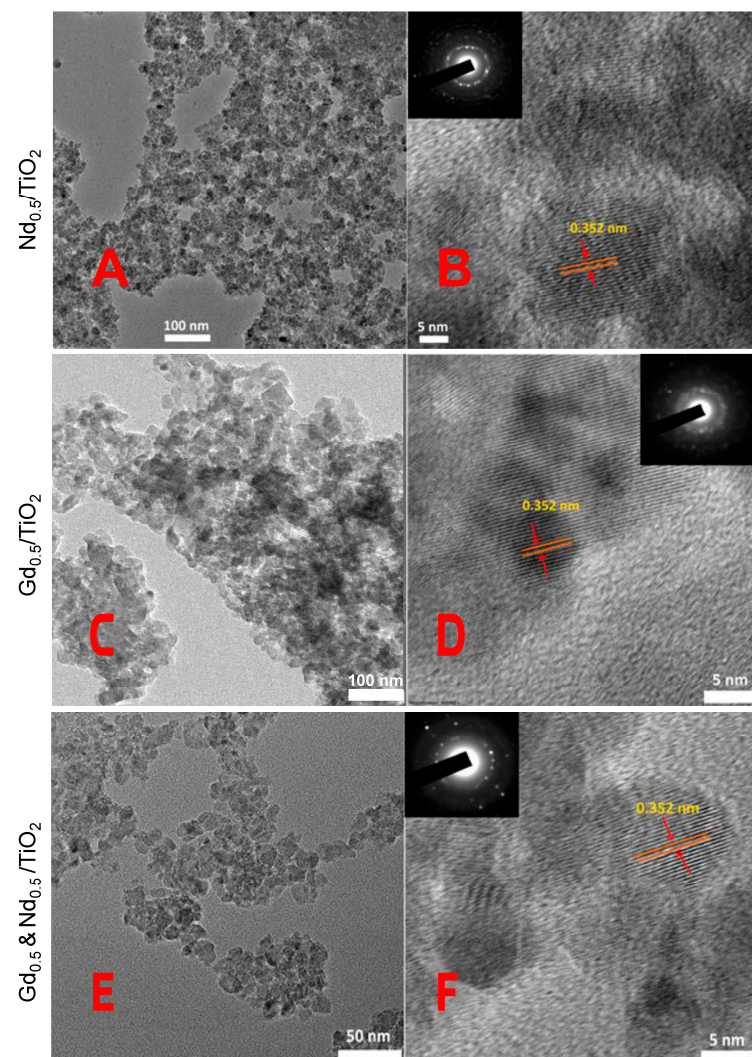
Figure 10. Transmission electron microscopy (TEM) and high-resolution TEM (HR-TEM) images (inset SAED patterns) of $Gd_{0.5}/TiO_2$, $Nd_{0.5}/TiO_2$, and $Gd_{0.5}/Nd_{0.5}/TiO_2$ (average particle size 12 ± 0.50 nm). (**A,B**) $Gd_{0.5}/TiO_2$, (**C,D**) $Nd_{0.5}/TiO_2$, and (**E,F**) $Gd_{0.5}/Nd_{0.5}/TiO_2$.

To estimate the optical band gap, UV-vis diffuse reflectance spectra were measured to analyze the red-shifts in the absorption regions. The Kubelka–Munk equation $\alpha h\nu = A(h\nu - E_g)^2$, where α, h, ν, and E_g and A are the absorption coefficient, Plank constant, light frequency, band gap, and the proportionality constant, respectively, was used for band gap determination, Figures 11 and 12. For pure TiO_2, a band gap energy of 3.18 eV was determined, which is in accordance with that of other reports [52–54], while for RE-doped TiO_2, the band gap energy decreased due to the red-shift of absorbance (see Figures 11 and 12 and Table 9), suggesting that gadolinium and neodymium improved the visible light absorbance of TiO_2.
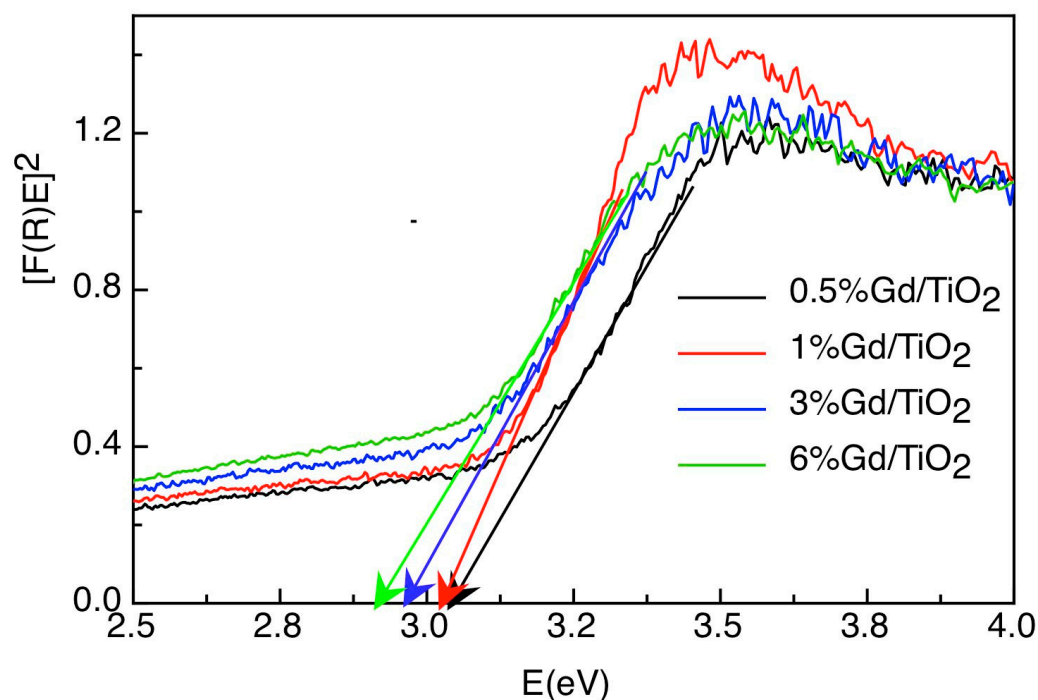

Figure 11. Kubelka–Munk function plots of Gd_x/TiO_2 NPs for different Gd atomic concentrations.

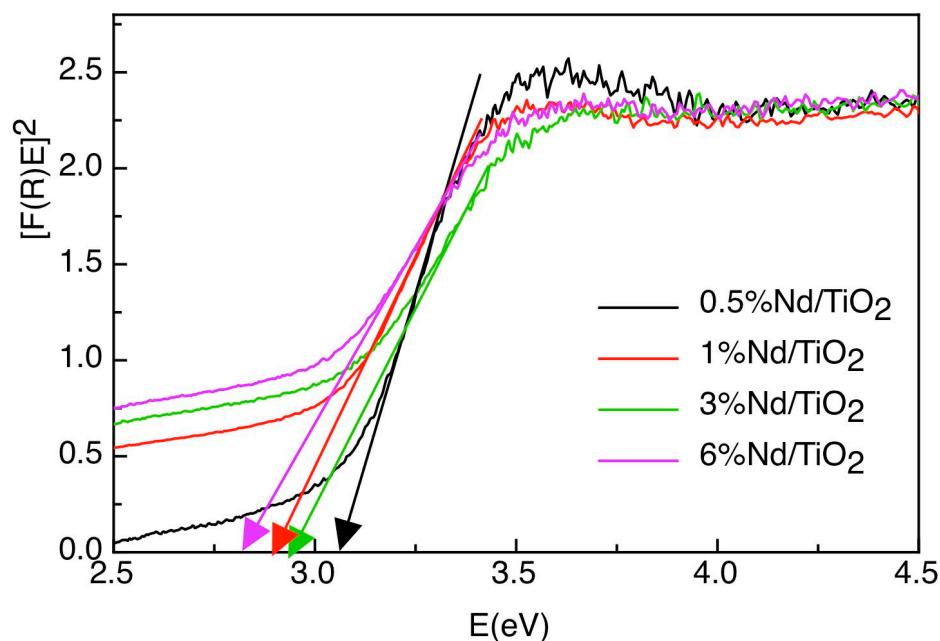**Figure 12.** Kubelka–Munk function plots of Nd_x/TiO_2 NPs for different Nd atomic concentrations.

Table 9. Band gaps of Gd_x/TiO_2 and Nd_x/TiO_2 NPs with different atomic concentrations.

	0.5%	1.0%	3.0%	6.0%
Gd_x/TiO_2	3.06	3.04	2.97	2.93
Nd_x/TiO_2	3.07	2.95	2.91	2.83

2.3. Electrocatalytic Activity Studies for the Hydrogen Evolution Reaction (HER)

2.3.1. Cathodic Polarization Measurements

Figure 13a presents the cathodic polarization plots of our synthesized catalysts, namely, Gd_x/TiO_2 and Nd_x/TiO_2 with various RE doping percentages (0.5, 1, 3, and 6%). The cathodic polarization curves of the $Gd_{1.0}/TiO_2$ NPs with varying Nd content, $Gd_{1.0}/Nd_x/TiO_2$ (x = 0.5, 1, 3, and 6%) were also recorded. Measurements were conducted in 1.0 M KOH solution in comparison with bare GCE and TiO_2/GCE. The polarization curves in Figure 13a also comprised the cathodic response of a commercial Pt/C catalyst as a reference point. The corresponding Tafel plots are exhibited in Figure 13b, and the fitting Tafel parameters are depicted in Table 10.
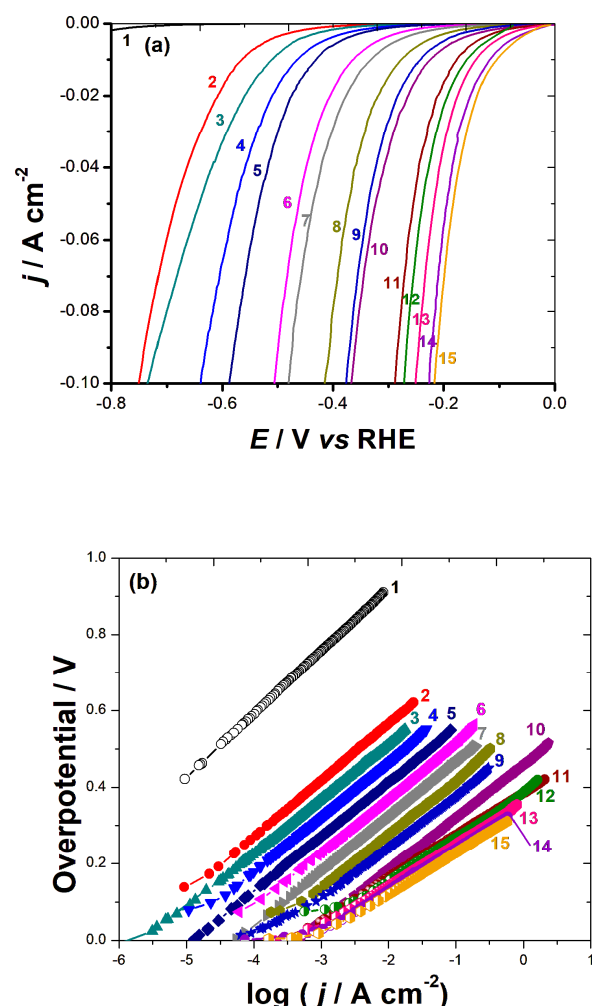
Figure 13. Cathodic polarization measurements for (**a**) the HER and (**b**) the corresponding Tafel plots recorded for the investigated catalysts. Measurements were carried out in 1.0 M KOH solution at a scan rate of 5 mV s^{-1} at room temperature. (1) bare GCE; (2) TiO_2/GCE; (3) $Gd_{0.5}/TiO_2$/GCE; (4) $Gd_{1.0}/TiO_2$/GCE; (5) $Gd_{3.0}/TiO_2$/GCE; (6) $Gd_{6.0}/TiO_2$/GCE; (7) $Nd_{0.5}/TiO_2$/GCE; (8) $Nd_{1.0}/TiO_2$/GCE; (9) $Nd_{3.0}/TiO_2$/GCE; (10) $Nd_{6.0}/TiO_2$/GCE; (11) $Gd_{1.0}/Nd_{0.5}/TiO_2$/GCE; (12) $Gd_{1.0}/Nd_{1.0}/TiO_2$/GCE; (13) $Gd_{1.0}/Nd_{3.0}/TiO_2$/GCE; (14) $Gd_{1.0}/Nd_{6.0}/TiO_2$/GCE; (15) Pt/C.

Table 10. Mean value (standard deviation) of the electrochemical HER kinetic parameters on the surfaces of our synthesized catalysts, Gd_x/TiO_2, Nd_x/TiO_2, and $Gd_{1.0}/Nd_x/TiO_2$ loaded on a GCE. Measurements were conducted at room temperature in deaerated KOH solution (1.0 M) in comparison with bare GCE, TiO_2/GCE, and Pt/C.

Tested Cathode	Onset Potential (E_{HER}, mV vs. RHE)	Tafel Slope (β_c, mV dec^{-1})	Exchange Current Density (j_o, mA cm^{-2})	Overpotential at j = 10 mA cm^{-2} (η_{10}, mV)
bare GCE	−720 (9.2)	−165 (2.6)	2.75 (0.05) × 10^{-5}	----
TiO_2/GCE	−215 (3.6)	−152 (2.2)	1.45 (0.03) × 10^{-3}	565 (7.6)
$Gd_{0.5}/TiO_2/GCE$	−186 (3.2)	−142 (1.7)	2.51 (0.04) × 10^{-3}	511 (6.2)
$Gd_{1.0}/TiO_2/GCE$	−175 (2.9)	−143 (1.8)	5.4 (0.15) × 10^{-3}	466 (5.1)
$Gd_{3.0}/TiO_2/GCE$	−160 (2.8)	−141 (2.1)	1.12 (0.3) × 10^{-2}	432 (4.7)
$Gd_{6.0}/TiO_2/GCE$	−145 (2.9)	−142 (1.8)	2.51 (0.04) × 10^{-2}	365 (4.2)
$Nd_{0.5}/TiO_2/GCE$	−130 (2.2)	−140 (1.5)	5.62 (0.06) × 10^{-2}	332 (3.8)
$Nd_{1.0}/TiO_2/GCE$	−118 (2.4)	−139 (1.5)	10.5 (0.3) × 10^{-2}	277 (3.5)
$Nd_{3.0}/TiO_2/GCE$	−103 (1.5)	−141 (1.6)	15.9 (0.42) × 10^{-2}	244 (3.2)
$Nd_{6.0}/TiO_2/GCE$	−85 (1.4)	140 (1.5)	43.6 (0.6) × 10^{-2}	225 (2.2)
$Gd_{1.0}/Nd_{0.5}/TiO_2/GCE$	−72 (1.6)	113 (1.4)	35.5 (0.4) × 10^{-2}	177 (1.9)
$Gd_{1.0}/Nd_{1.0}/TiO_2/GCE$	−60 (1.1)	112 (1.4)	44.7 (0.6) × 10^{-2}	161 (1.8)
$Gd_{1.0}/Nd_{3.0}/TiO_2/GCE$	−38 (0.8)	110 (1.8)	50.2 (0.7) × 10^{-2}	142 (1.7)
$Gd_{1.0}/Nd_{6.0}/TiO_2/GCE$	−22 (0.3)	109 (1.5)	72 (1.1) × 10^{-2}	115 (1.8)
Pt/C	−15 (0.2)	−106 (1.2)	80 (0.9) × 10^{-2}	106 (1.5)

As a well-known eminent HER electrocatalyst, the Pt/C catalyst achieved amongst the investigated catalysts the lowest HER's onset potential, E_{HER}~−15 mV vs. RHE, with the steepest reduction (catalytic) currents. In contrast, the bare GC electrode displayed inferior catalytic activity, clear from its humble catalytic current generated at a larger E_{HER} (−720 mV vs. RHE).

On the other hand, there was a substantial improvement in the HER catalytic activity in the reductive sweep curves of the synthesized Gd_x/TiO_2, Nd_x/TiO_2, and $Gd_{1.0}/Nd_x/TiO_2$ nanocomposites. This enhanced HER catalytic activity occurred to different extents depending on the type of studied catalyst, RE doping percentage and the bimetallic nanocomposite $Gd_{1.0}/Nd_x/TiO_2$ composition.

It follows, from Figure 13a, that the HER catalytic activity of Nd_x/TiO_2 and Gd_x/TiO_2 catalysts enhanced with RE doping percentage. In addition, at any RE doping percentage, the Nd_x/TiO_2 electrocatalyst exhibited higher HER activity than Gd_x/TiO_2. This was evident from their E_{HER} values recorded in Table 10. For instance, at a doping percentage of 3.0%, an E_{HER} value of −103 mV vs. RHE was recorded for $Nd_{3.0}/TiO_2$, which is 57 mV more anodic (active direction) than that of the $Gd_{3.0}/TiO_2$ catalyst (160 mV vs. RHE). The lower E_{HER} values of the Nd_x/TiO_2 catalysts led to higher exchange current density values, j_o. For example, a j_o value of 15.9 × 10^{-2} mA cm^{-2} was recorded for the $Nd_{3.0}/TiO_2$ catalyst. This $Nd_{3.0}$-TiO_2 catalyst's j_o value is ~14.2 times greater than that measured for the $Gd_{3.0}/TiO_2$ catalyst (1.12 × 10^{-2} mA cm^{-2}). The higher HER catalytic activity of Nd_x/TiO_2 catalysts was also testified from their lower overpotentials required to generate a current density of 10 mA cm^{-2}, η_{10}. For example, the $Nd_{3.0}/TiO_2$ catalyst required an η_{10} of 244 mV to deliver a current density of 10 mA cm^{-2}, which is 188 mV anodic to that attained by $Gd_{3.0}/TiO_2$ (432 mV).

These results highlight the high HER catalytic efficiency of the Nd_x/TiO_2 catalyst. The high Nd_x/TiO_2 electrocatalyst's HER activity compared to that of the Gd_x/TiO_2

electrocatalysts can be chiefly attributed to, as evidenced from XRD studies (revisit Table 3), the former's smaller crystallite size (~10 nm) than that of the latter (~20 nm). The Nd_x/TiO_2 electrocatalyst's smaller crystallite size is translated into higher electrochemical active surface area (EASA), as estimated from cyclic voltammetry measurements performed at various potential scan rates (Figure S3, Supporting Information).

The HER catalytic performance of the investigated $Gd_{1.0}/Nd_x/TiO_2$ bimetallic NPs (x = 0.5, 1, 3, and 6%) is positioned far beyond that of their corresponding individuals at any studied RE doping percentage, namely, Gd_x/TiO_2 and Nd_x/TiO_2 (x = 0.5, 1, 3, and 6%). In addition, the $Gd_{1.0}/Nd_x/TiO_2$ bimetallic NPs' catalytic activity for the HER was enhanced with increasing Nd content, approaching that of the commercial Pt/C electrocatalyst at a composition of $Gd_{1.0}/Nd_{6.0}/TiO_2$. This was evident from the E_{HER} and η_{10} values recorded for the tested $Gd_{1.0}/Nd_x/TiO_2$ bimetallic NPs, Table 10, that shift towards a more anodic direction with an increase in the Nd content. Thus, high cathodic currents, and hence large amounts of H_2, could be generated at low overpotentials, denoting efficacious catalytic performance for the HER.

Increasing the Nd doping percentage in the $Gd_{1.0}/Nd_x/TiO_2$ bimetallic NPs from x = 0.5 up to 6.0% has also led to higher j_o values, which represents another line of evidence for improved catalytic performance for the HER. The kinetics of the HER became therefore faster if both Gd and Nd NPs were combined as bimetallic, $Gd/Nd/TiO_2$, rather than individually loaded on TiO_2, i.e., Gd/TiO_2 and Nd/TiO_2. Another supported bimetallic NPs electrocatalysts, such as Au–Pd [27,28], Au–Ni [29], Cu–Pt [30], and porous Cu–Ti [55] exhibited analogous findings for the HER.

Bimetallic catalysts exhibit eminent catalytic characteristics, which are not observed in their individual monometallic counterparts, through cooperative interactions (synergistic effects) [27–30,55]. Such catalytic characteristics comprise increased electrocatalytic activity, improved chemical/physical stability, a greater surface area, and increased catalyst selectivity. On these grounds, the HER catalytic activity of our synthesized TiO_2-supported bimetallic Gd/Nd catalyst is possibly a result of the synergistic effect between Gd and Nd, abundant catalytically active sites, and an increasingly accessible electrochemical surface area. The increased accessible electrochemical surface area of the investigated bimetallic catalysts, namely, $Gd_{1.0}/Nd_{0.5}/TiO_2$, $Gd_{1.0}/Nd_{1.0}/TiO_2$, $Gd_{1.0}/Nd_{3.0}/TiO_2$, and $Gd_{1.0}/Nd_{6.0}/TiO_2$ catalysts compared with their individual monometallic counterparts (Gd/TiO_2 and Nd/TiO_2) was evidenced from cyclic voltammetry measurements (Figure S3, Supporting Information).

As revealed from Table 10, the $Gd_{1.0}/Nd_{6.0}/TiO_2$ bimetallic nanocomposite, the best catalyst here, exhibited E_{HER}, η_{10}, and j_o values of −22 mV vs. RHE, −109 mV dec^{-1}, and 0.72 mA cm^{-2}, respectively. These HER electrochemical kinetic parameter values are very close to those measured for the commercial Pt/C (−15 mV vs. RHE, −106 mV dec^{-1}, and 0.8 mA cm^{-2}). These findings reflect the outstanding HER catalytic performance of $Gd_{1.0}/Nd_{6.0}/TiO_2$ electrocatalyst that surpassed many effective electrocatalysts and are comparable with the most efficient ones reported in the literature (Table S1, Supporting Information).

An additional substantial electrochemical parameter, the Tafel slope, was also employed to assess and compare the HER catalytic efficiency of the investigated catalysts. In order to identify the major HER mechanism over the studied catalysts under such alkaline conditions, the measured Tafel slope values (Table 10) are contrasted with the standard values depicted in Equations (1)–(3). Such equations constitute the HER path in alkaline electrolytes on a particular catalyst [56]. The first water dissociation step (Volmer step, Equation (1)) is unavoidably the subject of the HER process under alkaline conditions, as few protons are present in alkaline electrolytes [56]. Following the Volmer step, either the two adsorbed hydrogen atoms are combined on the catalyst surface, forming a molecule H_2 (Tafel step, Equation (2)), or a hydrated proton is directly bonded to the adsorbed hydrogen

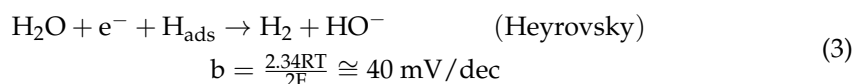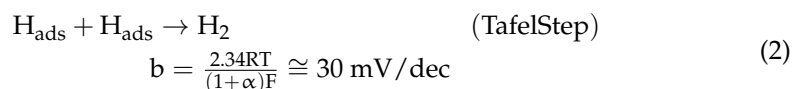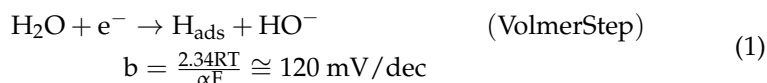atom that requires the transfer of the electron from the catalyst surface (Heyrovsky step, Equation (3)).

$$H_2O + e^- \rightarrow H_{ads} + HO^- \qquad \text{(VolmerStep)}$$
$$b = \frac{2.34RT}{\alpha F} \cong 120 \text{ mV/dec} \tag{1}$$

$$H_{ads} + H_{ads} \rightarrow H_2 \qquad \text{(TafelStep)}$$
$$b = \frac{2.34RT}{(1+\alpha)F} \cong 30 \text{ mV/dec} \tag{2}$$

$$H_2O + e^- + H_{ads} \rightarrow H_2 + HO^- \qquad \text{(Heyrovsky)}$$
$$b = \frac{2.34RT}{2F} \cong 40 \text{ mV/dec} \tag{3}$$

Table 10 reports a Tafel slope value of 110 mV dec^{-1} for the commercial Pt/C catalyst, which is in accordance with that recorded in the literature [57]; a good proof of the accuracy of the electrochemical measurements is utilized here. The Tafel lines of all tested Gd$_x$/TiO$_2$ and Nd$_x$/TiO$_2$ catalysts are parallel to each other with Tafel slopes of around 140 mV dec^{-1}. With Tafel slopes ranging from 108 to 113 mV dec^{-1}, the three studied Gd$_{1.0}$/Nd$_x$/TiO$_2$ bimetallic catalysts' Tafel lines are parallel to that of the Pt/C catalyst (110 mV dec^{-1}). The obvious decrease in the Tafel slope value from about 140 mV dec^{-1} for Gd$_x$/TiO$_2$ and Nd$_x$/TiO$_2$ catalysts to about 110 mV dec^{-1} for the four tested Gd$_{1.0}$/Nd$_x$/TiO$_2$ bimetallic catalysts adds another line of evidence for the enhanced HER kinetics on Gd$_{1.0}$/Nd$_x$/TiO$_2$ bimetallic catalyst surfaces. The explanation for this is that lower Tafel slopes usually indicate an abundance of active sites on the catalyst surface [58]. This result suggests an alkaline HER mechanism on the surface of the three studied bimetallic electrocatalysts that is similar to that taking place on the commercial Pt/C electrocatalyst. The Volmer step as the rate limiting step for the HER is part of that mechanism [57].

The catalysts' electrochemical active surface area (EASA) is another important metric used to compare their catalytic activity [59]. The inaccurate estimation of the specific capacitance of the composites, however, made it extremely difficult to quantify EASA for binary and ternary catalysts [60]. As a result of this, an alternative technique for assessing the catalytic activity of electrocatalysts is based on their electrochemical double-layer capacitance (C_{dl}), which has a direct link with EASA [61]. The values of C_{dl} (Table 11) were calculated in this investigation using cyclic voltammetry (CV) measurements performed at various potential sweep rates, as mentioned in Section S1 (Supporting Information).

Table 11. Estimated values for the examined electrocatalysts' double-layer capacitance (C_{dl}), electrochemical active surface area (EASA), net voltammetry charge (Q), and number of active sites (n) based on CV measurements, Figure S3 (Supporting Information).

Tested Cathode	$C_{dl}/$ $\mu F\ cm^{-2}$	EASA/cm^2	$Q \times 10^3$/C	$n \times 10^8$/mol
TiO$_2$ NPs alone	4.08	136.0	3.2	1.66
Gd$_{0.5}$/TiO$_2$	8.26	275.3	7.3	3.78
Gd$_{1.0}$/TiO$_2$	21.2	706.7	11.6	6.01
Gd$_{3.0}$/TiO$_2$	28.8	960.0	25.2	13.06
Gd$_{6.0}$/TiO$_2$	36.4	1213.3	34.5	17.88
Nd$_{0.5}$/TiO$_2$	21.8	726.7	10.8	5.60
Nd$_{1.0}$/TiO$_2$	29.9	996.7	15.4	7.98
Nd$_{3.0}$/TiO$_2$	38.6	1286.7	31.7	16.43
Nd$_{6.0}$/TiO$_2$	46.9	1563.3	41.2	21.35
Gd$_{1.0}$/Nd$_{0.5}$/TiO$_2$	39.2	1306.7	22.9	11.87
Gd$_{1.0}$/Nd$_{1.0}$/TiO$_2$	47.4	1580.0	43.5	22.54
Gd$_{1.0}$/Nd$_{3.0}$/TiO$_2$	55.6	1853.3	48.6	25.19
Gd$_{1.0}$/Nd$_{6.0}$/TiO$_2$	62.9	2096.7	56.8	29.43
Pt/C	65.4	2180.0	59.7	30.94

The results in Table 11 clearly showed that the C_{dl} values rose as the tested NPs' doping % in TiO_2 increased, with Nd NPs being more efficient than Gd NPs at every doping percentage examined. Depending on the amount of Nd in the $Gd_{1.0}/Nd_x/TiO_2$, the C_{dl} values further increased when Nd was co-doped with Gd. The obtained results demonstrated the catalytic influence of the synergistic interaction between Gd and Nd, as well as the abundance of catalytically active sites and a rising amount of accessible electrochemical surface area [27–30].

The surface sites that can be exploited for adsorption and desorption processes are more accessible and catalytically active in catalysts with higher C_{dl} values [62].

The value of EASA was calculated from C_{dl} using Equation (4) [62]:

$$EASA = C_{dl}/C_s \tag{4}$$

where C_s is the specific capacitance for an electrode with 1.0 cm^2 of flat, uniform surface area; it is typically between 20 and 40 mF cm^{-2}. Table 11 summarizes the EASA values calculated for the materials under investigation using a flat electrode with an average value of 30 mF cm^{-2}.

At any measured RE doping %, the $Gd_{1.0}/Nd_x/TiO_2$ bimetallic NPs clearly achieved EASA values higher than those of their equivalent individuals, thus confirming the cooperative interactions (synergistic effects) between Gd and Nd in catalyzing the HER [27–30]. The highly active surface area of the $Gd_{1.0}/Nd_x/TiO_2$ catalysts (1307, 1580, 1853, and 2097 cm^2 for x = 0.5, 1.0, 3.0, and 6.0%, respectively) might have contributed to the appreciable rise in their C_{dl} values (39.2, 47.4, 55.6, and 62.9 mF cm^{-2} for x = 0.5, 1.0, 3.0, and 6.0%, respectively).

Cyclic voltammetry data, Figure S3, and Equation (5) [63], were employed to estimate the number of active sites *n* for the investigated materials.

$$n = Q/2F \tag{5}$$

where *F* is the Faraday constant (96,485 C mol^{-1}) and 2 denotes the stoichiometric number of electrons that the HER of the electrode consumes. The studied $Gd_{1.0}/Nd_x/TiO_2$ bimetallic NPs (x = 0.5, 1.0, 3.0, and 6%) clearly displayed *n* values higher than those of their equivalent individual counterparts at any investigated RE doping percentage, namely, Gd_x/TiO_2 and Nd_x/TiO_2 (x = 0.5, 1.0, 3.0, and 6%). With increasing Nd content in the $Gd_{1.0}/Nd_x/TiO_2$ bimetallic NPs, the value of *n* increased approaching that computed for the commercial Pt/C electrocatalyst ($n = 30.94 \times 10^{-8}$ mol^{-1}) at a composition of Gd(1.0)-Nd (6.0), $n = 29.43 \times 10^{-8}$ mol^{-1}. These results confirmed the higher HER kinetics when the Gd and Nd NPs were combined into a hybrid bimetallic NP, $Gd_{1.0}/Nd_x/TiO_2$.

2.3.2. Faradaic Efficiency Calculations for the HER

The investigated catalysts' HER Faradaic efficiency (%) values were also calculated in order to further assess and compare their electrocatalytic activity. A controlled galvanostatic electrolysis was conducted to measure the amount of H_2 gas evolved (V_m, in mol) per hour using gas chromatography (GC), as reported in Section S4 (CGE), Equation (6).

$$V_m = \text{mol gas (GC)} \tag{6}$$

The value of V_c, the predicted amount of the released gas based on the charge transferred, is then computed using Equation (7) [64], assuming 100% Faradaic efficiency during the employed CGE:

$$V_c = Q(CGE)/nF \tag{7}$$

where *F* is the Faraday constant (96,485 C), $Q(CGE)$ is a representation of the charge transferred through the WE during the CGE operation, and *n* ($2H^+ + 2e = H_2$, $n = 2$) is a mathematical representation of the number of electrons exchanged during the HER. The value of

ε is derived by dividing V_m by V_c. The measured electrocatalyst's Faradaic efficiency (ε%) is then calculated by multiplying the ratio (V_m/V_c) quotient by 100, Equation (8) [64].

$$\text{Faradaic efficiency } (\varepsilon\%) = [Fn \text{ (mol gas(GC))}100]/Q\text{(CGE)} \tag{8}$$

The calculated and measured quantities of H_2 evolved for the examined electrocatalysts during the first hour of CGE are summarized in Table 12, which revealed that the tested $Gd_{1.0}/Nd_x/TiO_2$ bimetallic NPs, x = 1.0 and 6%, exhibited ε% values that are much higher than those of their equivalent individuals at any studied RE doping percentage, Gd_x/TiO_2 and Nd_x/TiO_2 (x = 1.0 and 6%). Additionally, it was also noticed that as Nd content was increased in $Gd_{1.0}/Nd_x/TiO_2$ from 1.0 to 6.0%, the HER's ε% value also enhanced from 92.9 to 98.7%, thus approaching that of the commercial Pt/C electrocatalyst (99.5%). These results provided another piece of evidence for the enhanced HER kinetics when both Gd and Nd dopants were brought together on TiO_2, forming the $Gd_{1.0}/Nd_x/TiO_2$ bimetallic NPs rather than being loaded separately, i.e., $Gd_{1.0}/TiO_2$ and Nd_x/TiO_2.

Table 12. Mean value (standard deviation) of V_{H2} (measured and calculated) obtained after 1 h of a controlled galvanostatic electrolysis (CGE) *, together with the Faradaic efficiency values, *FE* (%), for the studied catalysts.

Tested Catalyst	H$_2$ Measured by GC (H$_2$/µmol h^{-1})	Calculated H$_2$ Based on the Charge Passed during Electrolysis		*FE* (%)
		Charge Passed/C	H$_2$/µmol h^{-1}	
TiO$_2$ NPs alone	6.9 (0.12)	2.4 (0.05)	12.4 (0.2)	55.4 (0.8)
Gd$_{1.0}$/TiO$_2$	11.8 (0.15)	3.1 (0.055)	15.9 (0.31)	74.2 (1.1)
Gd$_{6.0}$/TiO$_2$	15.6 (0.3)	3.6 (0.06)	18.7 (0.38)	83.6 (1.3)
Nd$_{1.0}$/TiO$_2$	14.3 (0.26)	3.4 (0.052)	17.8 (0.35)	80.5 (1.2)
Nd$_{6.0}$/TiO$_2$	20.1 (0.35)	4.3 (0.07)	22.4 (0.4)	89.8 (1.5)
Gd$_{1.0}$/Nd$_{1.0}$/TiO$_2$	22.9 (0.4)	4.8 (0.09)	24.6 (0.42)	92.9 (1.4)
Gd$_{1.0}$/Nd$_{6.0}$/TiO$_2$	31.4 (0.55)	6.1 (0.12)	31.8 (0.5)	98.7 (1.6)
Pt/C	32.9 (0.3)	6.4 (0.1)	33.1 (0.36)	99.5 (1.4)

* CGE: the catalyst is held at a current density of -10 mA cm^{-2} for 1 h in 1.0 M KOH solution at 25 °C.

2.4. Best Catalyst's Long-Term Stability Tests

Excellent electrocatalysts must meet a number of criteria, one of which is long-term stability. To assess the stability of the best catalyst for the HER, two main electrochemical approaches were used. They comprise 72 h of controlled potential electrolysis (chronoamperometry) measurements as well as continuous (repetitive) cyclic polarization (CP) up to 10,000 cycles, Figure 14.

It follows from the CP measurements, Figure 14, that the catalyst's polarization curve maintained a high degree of similarity with just minor current losses after 10,000 cycles, thusreflecting good stability in the catalytic activity. CP findings were validated by electrolysis results at a static overpotential (inset of Figure 14); the current remained essentially constant during the run.
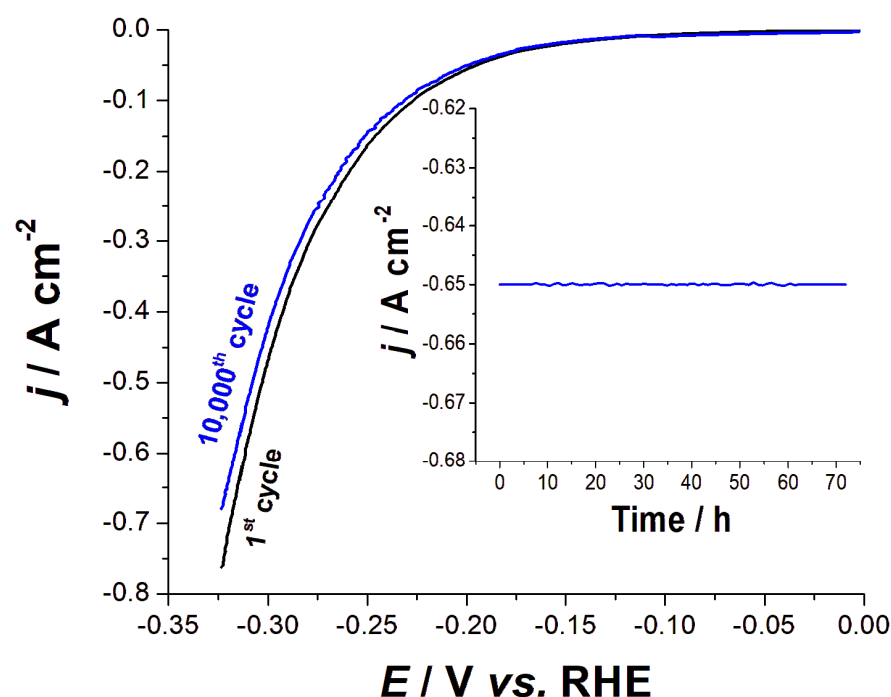
Figure 14.　Long-term stability tests recorded for the best performing electrocatalyst $(Gd_{1.0}/Nd_{6.0}/TiO_2)$ in 1.0 M KOH solution at room temperature for the HER. LSV measurements were conducted at a scan rate of 50 mV s^{-1}. Insets are chronoamperometry measurements (j vs. t) performed on the catalyst at a constant applied potential of -0.32 V vs. RHE.

3. Experimental

3.1. Synthesis of Gd^{3+}- or Nd^{3+}- as Well as 0.5%Gd^{3+}-0.5%Nd^{3+}-Doped TiO$_2$ NPs

Nanocrystalline TiO$_2$ nanoparticles (NPs) doped with different atomic concentrations (0.5, 1.0, 3.0, and 6.0%) of Gd^{3+} and Nd^{3+} ions were prepared adopting our previous method for the synthesis of pure TiO$_2$ nanoparticles [51]. The obtained materials were referred to as x% Gd or x% Nd-doped TiO$_2$, where %x is the percent content of Gd^{3+} or Nd^{3+} ions in the sample. Mixed 0.5%Gd^{3+}-0.5%Nd^{3+}-doped TiO$_2$ NPs were also obtained by the same method using a mass ratio of 0.5% of both Gd^{3+} and Nd^{3+} ions.

3.2. Electrocatalytic Activity Measurements
Electrochemical Setup

Electrochemical characterizations were carried out using a standard double-jacketed three-electrode electrochemical cell. A graphite rod (99.999% pure, Sigma-Aldrich, Darmstadt, Germany) and mercury/mercury oxide, Hg/HgO, NaOH(0.1 M), served as the cell's auxiliary and reference electrodes, respectively. The working electrode was a 3 mm glassy carbon (GC) loaded with catalyst (WE). Section S2 of the Supporting Information file gives the full description of the WE preparation for electrochemical experiments.

To evaluate the performance and stability of the synthesized electrocatalysts toward the HER, various electrochemical techniques were used, as reported in Section S3 (Supporting Information).

The electrochemically active surface area (EASA) of the catalysts was estimated using cyclic voltammetry (CV) tests carried out at various potential scan rates (ν: 20–120 mV s^{-1}) covering the potential range (0.32–0.42 V vs. RHE), which only permits the capacitive current to flow. The catalyst C_{dl} can be determined by plotting the difference in current density between anodic and cathodic scans ($\Delta J = J_{anodic} - J_{cathodic}$) against the slope of the ΔJ vs. ν plot at 0.37 V vs. RHE.

4. Conclusions

In this work, a facile and efficient one-pot method for the synthesis of RE^{3+} (Gd^{3+} or Nd^{3+})-doped TiO_2 NPs with different atomic concentrations (ca. 0.5–6.0%), namely, Gd_x/TiO_2, Nd_x/TiO_2, and $Gd_{1.0}/Nd_x/TiO_2$ bimetallic NPs, x = 0.5, 1.0, 3.0, and 6%, as efficient cathode materials for H_2 production, was developed. The structure and morphology of the obtained materials were characterized by using various techniques, which indicated that the prepared RE-doped TiO_2 NPs were pure-phase and uniformly dispersed. The crystallite size was about 20 nm in the case of Gd^{3+}-doping, while doping with Nd^{3+} decreased the crystallite size to about 10 nm. Linear cathodic polarization measurements were used to examine the as-prepared NPs as active electrocatalysts for effective hydrogen generation in alkaline solution (1.0 M KOH). The studied TiO_2-doped bimetallic NPs, namely, $Gd_{1.0}/Nd_x/TiO_2$, x = 0.5, 1.0, 3.0, and 6%, showed higher HER catalytic performance than their corresponding individual counterparts at any tested RE doping percentage, namely, Gd_x/TiO_2 and Nd_x/TiO_2. The $Gd_{1.0}/Nd_x/TiO_2$ HER catalytic performance was enhanced with increasing Nd content from 0.5 up to 6.0%. The $Gd_{1.0}/Nd_x/TiO_2$ maximum HER catalytic activity was attained at x = 6% with HER electrochemical kinetic parameters (onset potential: −22 mV, Tafel slope: 109 mV dec^{-1}, and exchange current density: 0.72 mA cm^{-2}), approaching the performance of the commercial Pt/C electrocatalyst (onset potential: −15 mV, Tafel slope: 106 mV dec^{-1}, and exchange current density: 0.80 mA cm^{-2}). The synergistic interaction of Gd and Nd is thought to be the major cause of the bimetallic catalyst's activity. The simplicity and originality of the procedure adopted here to synthesize such hybrid NPs, together with their high HER catalytic activity in the dark, are the fundamental features of this work.

Supplementary Materials: The following supporting information can be downloaded at: https://www.mdpi.com/article/10.3390/catal13081192/s1, Figure S1. FT-IR spectra of DMSO, Gd3+.nBuO, and Gd-doped TiO_2 NPs before (red) and after (blue) annealing process; Figure S2. TGA-DTA curves of Gdx-doped TiO_2 NPs recorded from room temperature to 1000 °C before (a) and after (b) calcination; Figure S3. Cyclic voltammograms recorded for studied catalysts at various potential scan rates (20–100 mV s^{-1}) measured in a non-Faradaic region of the voltammograms. Measurements were conducted in deaerated KOH solution (1.0 M) at room temperature; Figure S4. Double-layer capacitance measurements for determining the electrochemically-active surface area of Gdx/TiO_2 N and Ndx/TiO_2 N (x = 0.5, 1.0, 3.0, and 6.0 %) catalysts; Figure S5. Double-layer capacitance measurements for determining the electrochemically-active surface area of Gd1.0/Ndx/TiO_2 N (x = 0.5, 1.0, 3.0, and 6.0 %) catalysts; Table S1: Comparison of HER catalytic activity of our best performing electrocatalysts with the highly efficient ones reported in the literature in alkaline solutions [65–87].

Author Contributions: Conceptualization, M.A., N.A.A. and H.M.O.A.-M.; methodology, S.I.A., M.R.D. and A.A.S.; software (XRD, XRF, and XPS) and formal analysis, H.M.O.A.-M.; investigation, M.A. and N.A.A.; resources, M.A.A. and M.M.I.; data curation, M.A., R.B., M.A.A. and M.M.I.; writing—original draft preparation, A.A.S., M.A.A. and M.M.I.; writing—review and editing, M.A.A. and M.M.I.; visualization, M.A.A. and M.M.I.; supervision, M.A., M.A.A. and M.M.I.; project administration, M.A.; funding acquisition. All authors have read and agreed to the published version of the manuscript.

Conflicts of Interest: The authors declare no conflict of interest.

References

1. Morales-Guio, C.G.; Stern, L.A.; Hu, X. Nanostructured hydrotreating catalysts for electrochemical hydrogen evolution. *Chem. Soc. Rev.* **2014**, *43*, 6555–6569. [CrossRef]
2. Rostrup-Nielsen, J.R. Fuels and energy for the future: The role of catalysis. *Catal. Rev. Sci. Eng.* **2004**, *46*, 247–270. [CrossRef]
3. Tee, S.Y.; Win, K.Y.; Teo, W.S.; Koh, L.-D.; Liu, S.; Teng, C.P.; Han, M.-Y. Recent Progress in Energy-Driven Water Splitting. *Adv. Sci.* **2017**, *4*, 1600337. [CrossRef]
4. You, B.; Sun, Y. Innovative Strategies for Electrocatalytic Water Splitting. *Acc. Chem. Res.* **2018**, *51*, 1571–1580. [CrossRef]

5. Sapountzi, F.M.; Gracia, J.M.; Weststrate, C.J.; Fredriksson, H.O.A.; Niemantsverdriet, J.W. Electrocatalysts for the generation of hydrogen, oxygen and synthesis gas. *Prog. Energy Combust. Sci.* **2017**, *58*, 1–35. [CrossRef]

6. Yan, Y.; Xia, B.; Xu, Z.; Wang, X. Recent development of molybdenum sulfides as advanced electrocatalysts for hydrogen evolution reaction. *ACS Catal.* **2014**, *4*, 1693–1705. [CrossRef]

7. Faber, M.S.; Jin, S. Earth-abundant inorganic electrocatalysts and their nanostructures for energy conversion applications. *Energy Environ. Sci.* **2014**, *7*, 3519–3542. [CrossRef]

8. Xu, Y.; Zhang, B. Recent advances in porous Pt-based nanostructures: Synthesis and electrochemical applications. *Chem. Soc. Rev.* **2014**, *43*, 2439–2450. [CrossRef]

9. Roy, N.; Leung, K.T.; Pradhan, D. Nitrogen doped reduced graphene oxide-based Pt-TiO$_2$ nanocomposites for enhanced hydrogen evolution. *J. Phys. Chem. C* **2015**, *119*, 19117–19125. [CrossRef]

10. Esposito, D.V.; Hunt, S.T.; Kimmel, Y.C.; Chen, J.G. A new class of electrocatalysts for hydrogen production from water electrolysis: Metal monolayers supported on low-cost transition metal carbides. *J. Am. Chem. Soc.* **2012**, *134*, 3025–3033. [CrossRef]

11. Esposito, D.V.; Chen, J.G. Monolayer platinum supported on tungsten carbides as low-cost electrocatalysts: Opportunities and limitations. *Energy Environ. Sci.* **2011**, *4*, 3900–3912. [CrossRef]

12. Jiao, F.; Frei, H. Nanostructured cobalt and manganese oxide clusters as efficient water oxidation catalysts. *Energy Environ. Sci.* **2010**, *3*, 1018–1027. [CrossRef]

13. Merki, D.; Hu, X. Recent developments of molybdenum and tungsten sulfides as hydrogen evolution catalysts. *Energy Environ. Sci.* **2011**, *4*, 3878–3888. [CrossRef]

14. Padmapriya, S.; Harinipriya, S.; Sudha, V.; Kumar, D.; Pal, S.; Chaubey, B. Polyaniline coated copper for hydrogen storage and evolution in alkaline medium. *Int. J. Hydrogen Energy* **2017**, *42*, 20453–20462. [CrossRef]

15. Wang, J.; Gao, Y.; Kong, H.; Kim, J.; Choi, S.; Ciucci, F.; Hao, Y.; Yang, S.; Shao, Z.; Lim, J. Non-precious-metal catalysts for alkaline water electrolysis: Operando characterizations, theoretical calculations, and recent advances. *Chem. Soc. Rev.* **2020**, *49*, 9154–9196. [CrossRef]

16. Wang, J.; Kim, S.-J.; Liu, J.; Gao, Y.; Choi, S.; Han, J.; Shin, H.; Jo, S.; Kim, J.; Ciucci, F.; et al. Redirecting dynamic surface restructuring of a layered transition metal oxide catalyst for superior water oxidation. *Nat. Catal.* **2021**, *4*, 212–222. [CrossRef]

17. Wang, J.; Gao, Y.; Ciucci, F. Mechanochemical Coupling of MoS$_2$ and Perovskites for Hydrogen Generation. *ACS Appl. Energy Mater.* **2018**, *1*, 6409–6416. [CrossRef]

18. Chen, W.-F.; Sasaki, K.; Ma, C.; Frenkel, A.I.; Marinkovic, N.J.; Muckerman, T.; Zhu, Y.; Adzic, R.R. Hydrogen-evolution catalysts based on non-noble metal nickel-molybdenum nitride nanosheets. *Angew. Chem. Int. Ed.* **2012**, *51*, 6131–6135. [CrossRef]

19. Hsu, I.J.; Kimmel, Y.C.; Jiang, X.; Willis, B.G.; Chen, J.G. Atomic layer deposition synthesis of platinum-tungsten carbide core-shell catalysts for the hydrogen evolution reaction. *Chem. Commun.* **2012**, *48*, 1063–1065. [CrossRef]

20. Kong, D.; Wang, H.; Lu, Z.; Cui, Y. CoSe$_2$ nanoparticles grown on carbon fiber paper: An efficient and stable electrocatalyst for hydrogen evolution reaction. *J. Am. Chem. Soc.* **2014**, *136*, 4897–4900. [CrossRef]

21. Zhang, J.; Zhu, Z.; Tang, Y.; Muellen, K.; Feng, X. Titania nanosheet-mediated construction of a two-dimensional titania/cadmium sulfide heterostructure for high hydrogen evolution activity. *Adv. Mater.* **2014**, *26*, 734–738. [CrossRef] [PubMed]

22. Xu, H.; Yan, B.; Zhang, K.; Wang, J.; Li, S.; Wang, C.; Shiraishi, Y.; Du, Y.; Yang, P. Ultrasonicassisted synthesis of N-doped graphene-supported binary PdAu nanoflowers for enhanced electro-oxidation of ethylene glycol and glycerol. *Electrochim. Acta* **2017**, *245*, 227–236. [CrossRef]

23. Xu, H.; Zhang, K.; Yan, B.; Wang, J.; Wang, C.; Li, S.; Gu, Z.; Du, Y.; Yang, P. Ultrauniform PdBi nanodots with high activity towards formic acid oxidation. *J. Power Sources* **2017**, *356*, 27–35. [CrossRef]

24. Xu, H.; Yan, B.; Wang, J.; Zhang, K.; Li, S.; Xiong, Z.; Wang, C.; Shiraishi, Y.; Du, Y.; Yang, P. Self-supported porous 2D AuCu triangular nanoprisms as model electrocatalysts for ethylene glycol and glycerol oxidation. *J. Mater. Chem. A* **2017**, *5*, 15932–15939. [CrossRef]

25. Xu, H.; Wang, J.; Yan, B.; Zhang, K.; Li, S.; Wang, C.; Shiraishi, Y.; Du, Y.; Yang, P. Hollow AuxAg/Au core/shell nanospheres as efficient catalysts for electrooxidation of liquid fuels. *Nanoscale* **2017**, *9*, 12996–13003. [CrossRef]

26. Greeley, J.; Jaramillo, T.F.; Bonde, J.; Chorkendorff, I.; Norskov, J.K. Computational high-throughput screening of electrocatalytic materials for hydrogen evolution. *Nat. Mater.* **2006**, *5*, 909–913. [CrossRef]

27. Darabdhara, G.; Amin, M.A.; Mersal, G.A.M.; Ahmed, E.M.; Das, M.R.; Zakaria, M.B.; Malgras, V.; Alshehri, S.M.; Yamauchi, Y.; Szunerits, S.; et al. Reduced graphene oxide nanosheets decorated with Au, Pd and Au-Pd bimetallic nanoparticles as highly efficient catalysts for electrochemical hydrogen generation. *J. Mater. Chem. A* **2015**, *3*, 20254–20266. [CrossRef]

28. Totha, P.S.; Velicky, M.; Slater, T.J.A.; Worrall, S.D.; Haigh, S.J. Hydrogen evolution and capacitance behavior of Au/Pd nanoparticle-decorated graphene heterostructures. *Appl. Mater. Today* **2017**, *8*, 125–131. [CrossRef]

29. Darabdhara, G.; Das, M.R.; Amin, M.A.; Mersal, G.A.M.; Mostafa, N.Y.; Abd El-Rehim, S.S.; Szunerits, S.; Boukherroub, R. Au-Ni alloy nanoparticles supported on reduced graphene oxide as highly efficient electrocatalysts for hydrogen evolution and oxygen reduction reactions. *Int. J. Hydrogen Energy* **2018**, *43*, 1424–1438. [CrossRef]

30. Mandegarzad, S.; Raoof, J.B.; Hosseini, S.R.; Ojani, R. Cu-Pt bimetallic nanoparticles supported metal organic framework-derived nanoporous carbon as a catalyst for hydrogen evolution reaction. *Electrochim. Acta* **2016**, *190*, 729–736. [CrossRef]

31. Wang, L.; Qi, B.; Sun, L.; Sun, Y.; Guo, C.; Li, Z. Synthesis and assembly of Au-Pt bimetallic nanoparticles. *Mater. Lett.* **2008**, *62*, 1279–1282. [CrossRef]

32. Raoof, J.-B.; Ojani, R.; Rashid-Nadimi, S. Electrochemical synthesis of bimetallic Au@Pt nanoparticles supported on gold film electrode by means of self-assembled monolayer. *J. Electroanal. Chem.* **2010**, *641*, 71–77. [CrossRef]

33. Chen, Y.-L.; Xiong, L.; Song, X.-N.; Wang, W.-K.; Huang, Y.-X.; Yu, H.-Q. Electrocatalytic hydrodehalogenation of atrazine in aqueous solution by Cu/Pd/Ti catalyst. *Chemosphere* **2015**, *125*, 57–63. [CrossRef]

34. Li, S.S.; Wang, A.J.; Hu, Y.Y.; Fang, K.M.; Chen, J.R.; Feng, J.J. One-step, seedless wet-chemical synthesis of gold@palladium nanoflowers supported on reduced graphene oxide with enhanced electrocatalytic properties. *J. Mater. Chem. A* **2014**, *2*, 18177–18183. [CrossRef]

35. Ma, X.; Zhao, K.; Tang, H.; Chen, Y.; Lu, C.; Liu, W.; Gao, Y.; Zhao, H.; Tang, Z. New insight into the role of gold nanoparticles in Au@CdS core-shell nanostructures for hydrogen evolution. *Small* **2014**, *10*, 4664–4670. [CrossRef] [PubMed]

36. Lang, L.; Shi, Y.; Wang, J.; Wang, F.-B.; Xia, X.-H. Hollow core-shell structured Ni-Sn@C nanoparticles: A novel electrocatalyst for the hydrogen evolution reaction. *ACS Appl. Mater. Interfaces* **2015**, *7*, 9098–9102. [CrossRef]

37. ICDD. *PDF 2, Database Sets 1–45*; The International Centre for Diffraction Data: Newtown Square, PA, USA, 1995.

38. Lutterotti, L.; Scardi, P. Simultaneous structure and size-strain refinement by the Rietveld method. *J. Appl. Crystallogr.* **1990**, *23*, 246–252. [CrossRef]

39. Lutterotti, L. Total pattern fitting for the combined size–strain–stress–texture determination in thin film diffraction. *Nucl. Instrum. Methods Phys. Res. B* **2010**, *268*, 334–340. [CrossRef]

40. *ICSD Database, Version 2005-1*; Fachinformationszentrum Karlsruhe: Eggenstein-Leopoldshafen, Germany; U.S. Department of Commerce: Washington, DC, USA, 2005.

41. Vegard, L. The Constitution of Mixed Crystals and the Space Occupied by Atoms. *Z. Phys.* **1921**, *5*, 17–26. [CrossRef]

42. Wagner, C.D.; Gale, L.H.; Raymond, R.H. Two-dimensional chemical state plots: A standardized data set for use in identifying chemicalstates by X-ray photoelectron spectroscopy. *Anal. Chem.* **1979**, *51*, 466–482. [CrossRef]

43. Choi, J.; Sudhagar, P.; Lakshmipathiraj, P.; Lee, J.W.; Devadoss, A.; Lee, S.; Song, T.; Hong, S.; Eito, S.; Terashima, C.; et al. Three-dimensional Gd-doped TiO$_2$ fibrous photoelectrodes for efficient visible light-driven photocatalytic performance. *RSC Adv.* **2014**, *4*, 11750–11757. [CrossRef]

44. He, Y.-B.; Li, B.; Liu, M.; Zhang, C.; Lv, W.; Yang, C.; Li, J.; Du, H.; Zhang, B.; Yang, Q.H.; et al. Gassing in Li$_4$Ti$_5$O$_{12}$-based batteries and its remedy. *Sci. Rep.* **2012**, *2*, 913. [CrossRef]

45. Lyu, J.; Gao, J. Construction of homojunction-adsorption layer on anatase TiO$_2$ to improve photocatalyticmineralization of volatile organic compounds. *Appl. Catal. B* **2017**, *202*, 664–667. [CrossRef]

46. Wang, M.; Xu, X.; Lin, L.; He, D. Gd–La codoped TiO$_2$ nanoparticles as solar photocatalysts. *Prog. Nat. Sci.* **2015**, *35*, 6–11. [CrossRef]

47. Rengaraj, S.; Venkataraj, S.; Yeon, J.-W.; Kim, Y.; Li, X.Z.; Pang, G.K.H. Preparation, characterization and application of Nd–TiO$_2$ photocatalyst for the reduction of Cr(VI) under UV light illumination. *Appl. Catal. B* **2007**, *77*, 157–165. [CrossRef]

48. Yang, C.H.; Ma, Z.Q.; Li, F.; He, B.; Yuan, J.H.; Zhang, Z.H. Spectrum analysis on phase transformations in TiO$_2$ thin films. *Acta Phys.-Chim. Sin.* **2010**, *26*, 1349–1354.

49. Raiser, D.; Deville, J.P. Study of XPS photoemission of some gadolinium compounds. *J. Electron Spectrosc.* **1991**, *57*, 91–97. [CrossRef]

50. Wang, C.; Ao, Y.; Wang, P.; Hou, J.; Qian, J. Preparation, characterization and photocatalytic activity of the neodymium-doped TiO$_2$ hollow spheres. *Appl. Surf. Sci.* **2010**, *257*, 227–231. [CrossRef]

51. Ibrahim, M.M.; Mezni, A.; Alsawat, M.; Kumeria, T.; Das, M.R.; Alzahly, S.; Aldalbahi, A.; Gornicka, K.; Ryl, J.; Amin, M.A.; et al. Enhanced hydrogen evolution reaction on highly stable titania-supported PdO and Eu$_2$O$_3$ nanocomposites in a strong alkaline solution. *Int. J. Energy Res.* **2019**, *43*, 5367–5383. [CrossRef]

52. Mezni, A.; Ibrahim, M.M.; El-Kemary, M.; Shaltout, A.A.; Mostafa, N.Y.; Ryl, J.; Kumeria, T.; Altalhi, T.; Amin, M.A. Cathodically Activated Au/TiO$_2$ Nanocomposite Synthesized by a New Facile Solvothermal Method: An Efficient Electrocatalyst with Pt-like Activity for Hydrogen Generation. *Electrochim. Acta* **2018**, *290*, 404–418. [CrossRef]

53. Amin, M.A.; Ahmed, E.M.; Mostafa, N.Y.; Alotibi, M.M.; Darabdhara, G.; Das, M.R.; Wysocka, J.; Ryl, J.; Abd El-Rehim, S.S. Aluminum Titania Nanoparticle Composites as Nonprecious Catalysts for Efficient Electrochemical Generation of H$_2$. *ACS Appl. Mater. Interfaces* **2016**, *8*, 23655–23667. [CrossRef] [PubMed]

54. Ibrahim, M.M.; Mezni, A.; Alsawat, M.; Kumeria, T.; Alrooqi, A.; Shaltout, A.A.; Ahmed, S.I.; Boukherroub, R.; Amin, M.A.; Altalhi, T. Crystalline ZnO and ZnO/TiO$_2$ nanoparticles derived from *tert*-butyl N-(2 mercaptoethyl)carbamatozinc(II) chelate: Electrocatalytic studies for H$_2$ generation in alkaline electrolytes. *Int. J. Energy Res.* **2020**, *44*, 6725–6744. [CrossRef]

55. Lu, Q.; Hutchings, G.S.; Yu, W.; Zhou, Y.; Forest, R.V.; Tao, R.; Rosen, J.; Yonemoto, B.T.; Cao, Z.; Zheng, H.; et al. Highly porous non-precious bimetallic elec for efficient hydrogen evolution. *Nat. Commun.* **2015**, *6*, 6567. [CrossRef] [PubMed]

56. Mahmood, N.; Yao, Y.; Zhang, J.-W.; Pan, L.; Zhang, X.; Zou, J.-J. Electrocatalysts for Hydrogen Evolution in Alkaline Electrolytes: Mechanisms, Challenges, and Prospective Solutions. *Adv. Sci.* **2018**, *5*, 1700464. [CrossRef]

57. Durst, J.; Siebel, A.; Simon, C.; Hasche, F.; Herranz, J.; Gasteiger, H.A. New Insights into the Electrochemical Hydrogen Oxidation and Evolution Reaction Mechanism. *Energy Environ. Sci.* **2014**, *7*, 2255–2260. [CrossRef]

58. Shinagawa, T.; Garcia-Esparza, A.T.; Takanabe, K. Insight on Tafel Slopes from A Microkinetic Analysis of Aqueous Electrocatalysis for Energy Conversion. *Sci. Rep.* **2015**, *5*, 13801. [CrossRef]

59. Ito, Y.; Cong, W.T.; Fujita, T.; Tang, Z.; Chen, M.W. High Catalytic Activity of Nitrogen and Sulfur Co doped Nanoporous Graphene in the Hydrogen Evolution Reaction. *Angew. Chem. Int. Ed.* **2015**, *54*, 2131–2136. [CrossRef]

60. Zhang, H.C.; Li, Y.J.; Zhang, G.X.; Xu, T.H.; Wan, P.B.; Sun, X.M. A Metallic CoS2 Nanopyramid Array Grown on 3D Carbon Fiber Paper as an Excellent Electrocatalyst for Hydrogen Evolution. *J. Mater. Chem. A* **2015**, *3*, 6306–6310. [CrossRef]

61. Liu, N.; Guo, Y.; Yang, X.; Lin, H.; Yang, L.; Shi, Z.; Zhong, Z.; Wang, S.; Tang, Y.; Gao, Q. Microwave-Assisted Reactant-Protecting Strategy Toward Efficient MoS2 Electrocatalysts in Hydrogen Evolution Reaction. *ACS Appl. Mater. Interfaces* **2015**, *7*, 23741–23749. [CrossRef]

62. Kibsgaard, J.; Jaramillo, T.F. Molybdenum Phosphosulfide: An Active, Acid-Stable, Earth-Abundant Catalyst for the Hydrogen Evolution Reaction. *Angew. Chem. Int. Ed.* **2014**, *53*, 14433–14437. [CrossRef]

63. Liu, Y.-R.; Shang, X.; Gao, W.-K.; Dong, B.; Chi, J.-Q.; Li, X.; Yan, K.-L.; Chai, Y.-M.; Liu, Y.-Q.; Liu, C.-G. Ternary CoS2/MoS2/RGO Electrocatalyst with CoMoS Phase for Efficient Hydrogen Evolution. *Appl. Surf. Sci.* **2017**, *412*, 138–145. [CrossRef]

64. Beyene, B.B.; Mane, S.B.; Hung, C.-H. Highly efficient electrocatalytic hydrogen evolution from neutral aqueous solution by a water-soluble anionic cobalt(II) porphyrin. *Chem. Commun.* **2015**, *51*, 15067–15070. [CrossRef]

65. Head, D.; Mc Carty, G. Acetylation of N-isopropylideneanilines. Formation of a novel 1,3-oxazetidine derivative. *Tetrahedron Lett.* **1975**, *16*, 1405–1408.

66. Amine, A.; Imen, B.; Adnen, M.; Noureddine, J.; Leila, S. Hybrid Au-Fe3O4 Nanoparticles: Plasmonic, Surface Enhanced Raman Scattering, and Phase Transition Properties. *J. Phys. Chem. C* **2013**, *117*, 16166–16174.

67. Yang, C.; Tang, Y.H.; Lam, W.M.; Lu, W.W.; Gao, P.; Zhao, C.B.; Yuen, M.F. Moisture-cured elastomeric transparent UV and X-ray shielding organic–inorganic hybrids. *J. Mater. Sci.* **2010**, *45*, 588–3594. [CrossRef]

68. Velasco, M.J.; Rubio, F.; Rubio, J.; Oteo, J.L. Hydrolysis of Titanium Tetrabutoxide. Study by FT-IR Spectroscopy. *Spectrosc. Lett.* **1999**, *32*, 289–304. [CrossRef]

69. Mezni, A.; Kouki, F.; Romdhane, S.; Fonrose, B.; Joulie, S.; Mlayah, A.; Smiri, L. Facile Synthesis of Cu-doped ZnO Nanoparticle in Triethyleneglycol: Photocatalytic Activities and Aquatic Ecotoxicity. *Mater. Lett.* **2012**, *86*, 153–156. [CrossRef]

70. Que, W.; Zhou, Y.; Lam, Y.L.; Chan, Y.C.; Kam, C.H. Sol-gel Preparation and Optical Properties of TiO2/Organically Modified Silane Hybrid Material Containing DR13. *J. Sol–Gel. Sci. Technol.* **2001**, *20*, 187–195. [CrossRef]

71. Wang, B.L.; Hu, L.L. Polydimethylsiloxane/silica/titania composites prepared by solvent-free sol-gel technique. *Mater. Chem. Phys.* **2005**, *89*, 417–422. [CrossRef]

72. Vasilyeva, I.; Kuz'micheva, G.; Pochtar, A.; Gainanova, A.; Timaeva, O.; Dorokhov, A.; Podbel'skiy, V. On the nature of the phase "η-TiO2". *New J. Chem.* **2016**, *40*, 151–161. [CrossRef]

73. Ibrahim, M.M.; Mezni, A.; El-Sheshtawy, H.S.; Abu Zaid, A.A.; Alsawat, M.; El-Shafi, N.; Ahmed, S.I.; Shaltout, A.A.; Amin, M.A.; Kumeria, T.; et al. Direct Z-scheme of Cu2O/TiO2 enhanced self-cleaning, antibacterial activity, and UV protection of cotton fiber under sunlight. *Appl. Surf. Sci.* **2019**, *479*, 953–962. [CrossRef]

74. Wang, C.; Bilan, H.K.; Podlaha, E.J. Electrodeposited Co-Mo-TiO2 Electrocatalysts for the Hydrogen Evolution Reaction. *J. Electrochem. Soc.* **2019**, *166*, F661–F669. [CrossRef]

75. Laszczyńska, A.; Szczygieł, I. Electrocatalytic activity for the hydrogen evolution of the electrodeposited Co–Ni–Mo, Co–Ni and Co–Mo alloy coatings. *Int. J. Hydrogen Energy* **2020**, *45*, 508–520. [CrossRef]

76. Zhou, Y.; Luo, M.; Zhang, W.; Zhang, Z.; Meng, X.; Shen, X.; Liu, H.; Zhou, M.; Zeng, X. Topological Formation of a Mo–Ni-Based Hollow Structure as a Highly Efficient Electrocatalyst for the Hydrogen Evolution Reaction in Alkaline Solutions. *ACS Appl. Mater. Interfaces* **2019**, *11*, 21998–22004. [CrossRef]

77. Gao, M.Y.; Yang, C.; Zhang, Q.B.; Yu, Y.W.; Hua, Y.X.; Li, Y.; Dong, P. Electrochemical fabrication of porous Ni-Cu alloy nanosheets with high catalytic activity for hydrogen evolution. *Electrochim. Acta* **2016**, *215*, 609–616. [CrossRef]

78. Fang, M.; Gao, W.; Dong, G.; Xia, Z.; Yip, S.; Qin, Y.; Qu, Y.; Ho, J.C. Hierarchical NiMo-based 3D electrocatalysts for highly-efficient hydrogen evolution in alkaline conditions. *Nano Energy* **2016**, *27*, 247–254. [CrossRef]

79. Thenuwara, A.C.; Dheer, L.; Attanayake, N.H.; Yan, Q.; Waghmare, U.V.; Strongin, D.R. Co-Mo-P Based Electrocatalyst for Superior Reactivity in the Alkaline Hydrogen Evolution Reaction. *ChemCatChem* **2018**, *10*, 4846–4851. [CrossRef]

80. Zhang, C.; Chen, B.; Mei, D.; Liang, X. The OH$^-$-driven synthesis of Pt–Ni nanocatalysts with atomic segregation for alkaline hydrogen evolution reaction. *J. Mater. Chem. A* **2019**, *7*, 5475–5481. [CrossRef]

81. Rosalbino, F.; Macciò, D.; Saccone, A.; Angelini, E.; Delfino, S. Fe-Mo-R (R = rare earth metal) crystalline alloys as a cathode material for hydrogen evolution reaction in alkaline solution. *Int. J. Hydrogen Energy* **2011**, *36*, 1965–1973. [CrossRef]

82. Cabello, G.; Gromboni, M.F.; Pereira, E.C.; Mascaro, L.H.; Marken, F. Microwave-Electrochemical Deposition of a Fe-Co Alloy with Catalytic Ability in Hydrogen Evolution. *Electrochim. Acta* **2017**, *235*, 480–487. [CrossRef]

83. Liu, G.; Bai, H.; Ji, Y.; Wang, L.; Wen, Y.; Lin, H.; Zheng, L.; Li, Y.; Zhang, B.; Peng, H. A highly efficient alkaline HER Co–Mo bimetallic carbide catalyst with an optimized Mo d-orbital electronic state. *J. Mater. Chem. A* **2019**, *7*, 12434–12439. [CrossRef]

84. Yao, M.; Wang, B.; Sun, B.; Luo, L.; Chen, Y.; Wang, J.; Wang, N.; Komarneni, S.; Niu, X.; Hu, W. Rational design of self-supported Cu@WC core-shell mesoporous nanowires for pH-universal hydrogen evolution reaction. *Appl. Catal. B* **2021**, *280*, 119451. [CrossRef]

85. Ren, J.; Wang, Q.; Xiang, Q.; Yang, C.; Liang, Y.; Li, J.; Liu, J.; Qian, D. O-vacancy-rich and heterostructured Cu/Cu2O/NiO@NiCu foam self-supported advanced electrocatalyst towards hydrogen evolution: An experimental and DFT study. *Chem. Eng. Sci.* **2023**, *280*, 119026. [CrossRef]

86. Fu, H.; Zhang, N.; Lai, F.; Zhang, L.; Chen, S.; Li, H.; Jiang, K.; Zhu, T.; Xu, F.; Liu, T. Surface-regulated platinum–copper nanoframes in electrochemical reforming of ethanol for efficient hydrogen production. *ACS Catal.* **2022**, *12*, 11402–11411. [CrossRef]

87. Zhang, N.; Zhang, Q.; Xu, C.; Li, Y.; Zhang, J.; Wu, L.; Liu, Y.; Fang, Y.; Liu, Z. Optional construction of $Cu_2O@Fe_2O_3@CC$ architecture as a robust multifunctional photoelectronic catalyst for overall water splitting and CO_2 reduction. *Chem. Eng. J.* **2021**, *426*, 131192. [CrossRef]